Materials and Structures (2026) 59:394
https://doi.org/10.1617/s11527-026-03265-4

ORIGINAL ARTICLE

Structural performance of cement paste cylinders cured in microgravity on the ISS: effects of air-entraining agent and simulated microgravity conditions

J. T. I. Müller · T. Welsch · B. Rattenbacher · W. Walls · K. Tell · M. Schnellenbach-Held · M. Sperl

Received: 18 March 2026 / Revised: 6 July 2026 / Accepted: 27 August 2026 / Published online: 18 September 2026
© The Author(s) 2026

Abstract As humanity looks to the stars for future colonies, mastering the science of construction in space begins with a deep understanding of how materials perform in extraterrestrial environment. This study pioneers investigations of microgravity effects on cement paste bulk properties. Samples, produced in defined cylindrical shapes on the International Space Station (ISS), allowed for the first-time determination of macroscopic compressive strengths of microgravity samples. A thorough analysis revealed significant impacts on composition, density, and porosity, with compressive strength (−19%) and Young's modulus (−5.5%) lowered due to increased overall porosity (+12.3%). Unexpectedly, the addition of an air-entraining agent resulted in lower overall porosity (−8.7%) and higher compressive strength (+18.6%) in microgravity samples as compared to normal gravity (g) on earth. While this effect was consistent across the tests, the underlying cause remains unresolved. Ground-based microgravity simulators like the clinostat and the random positioning machine partially replicated microgravity effects, revealing the challenges of simulating actual microgravity. Achieving homogeneity and preventing large air voids require optimization of the manufacturing-concrete mixing processes, but nevertheless the findings underscore the feasibility of high-quality concrete production in microgravity.

Keywords Compressive strength · Curing · Microgravity · Pore size distribution · Porosity · Microgravity simulation · Air-entraining agent

Supplementary Information The online version contains supplementary material available at https://doi.org/10.1617/s11527-026-03265-4.

J. T. I. Müller (✉) · T. Welsch · M. Schnellenbach-Held
University of Duisburg-Essen (UDE) – Institute for Structural Concrete, Essen, Germany
e-mail: julian.mueller@uni-due.de

B. Rattenbacher
Lucerne University of Applied Sciences and Arts (HSLU) – BIOTESC, Lucerne, Switzerland

W. Walls · K. Tell · M. Sperl
German Aerospace Center (DLR) – Institute of Materials Physics in Space, Cologne, Germany

W. Walls · M. Sperl
University of Cologne (UoC) – Institute for Theoretical Physics, Cologne, Germany

1 Introduction

More than five decades following the Apollo 17 mission, NASA's Artemis program is dedicated to sending humans back to the Moon. The program focuses on establishing a sustained human presence on the lunar surface [1]. To allow a permanent presence on the moon, infrastructure like landing pads and habitats need to be established. Therefore, suitable building materials and building processes must

be identified that allow building in a low gravity and no-atmosphere environment. NASA's Moon-to-Mars Planetary Autonomous Construction Technology (MMPACT) project is currently investigating different approaches for autonomous construction in extraterrestrial environments, including construction methods based on cementitious materials [2].

Concrete is the most widely used building material on Earth, but it is unclear if it can compete in space. Some thoughts on the use of concrete for the construction of lunar habitats and space stations were already made at the end of the 1980s [3, 4]. The first concrete experiment in microgravity was carried out back in 1994 [5, 6]. During the shuttle flight (STS-68) one single cylindrical concrete sample should be produced. However, the piston in the mixing chamber, which was meant to compress the fresh mixture and reduce air voids, jammed mid-flight. As a result, the mixing was incomplete, and the concrete specimen had an irregular shape. Despite the issue, the test confirmed that microgravity significantly affects concrete behavior. Post-flight analysis revealed non-uniform density distribution and high air void content with irregular shaped and large air voids. Microstructural examination showed increased porosity and the formation of smaller, more irregular calcium silicate hydrate (C–S–H) and ettringite crystals compared to Earth-based samples. [8]

Much later, in 2014, experiments on early cement hydration and crystal growth were performed during parabolic flights, which provide 20–22 s of microgravity. Using a special setup with syringes and valves, hydration was initiated and stopped with acetone after 10 s. More ettringite crystals formed in microgravity, but they were smaller due to slower growth. A lack of convection was postulated as the cause for this phenomenon [9]. The addition of superplasticizer showed that polymers affect crystal size by adsorbing on ettringite surfaces [10]. The experiments also showed that calcium silicate hydrate (C–S–H) crystals were smaller but more numerous in microgravity than under normal gravity [10, 11].

Only recently, researchers from the Pennsylvania State University (PSU) systematically examined the solidification of cement paste components in microgravity on the International Space Station (ISS). As part of the Microgravity Investigations of Concrete Solidification (MICS) project, 120 samples from 16 different mixtures were produced, the most of them by the German ESA astronaut Alexander Gerst. The experiments covered diverse cement compositions, investigating hydration processes and crystal growth. In the first published study a tricalcium silicate (C_3S) paste with a high w/c ratio of 2.0 was analyzed [12]. It was demonstrated that microgravity affected crystal morphology of these samples and the Portlandite crystals grew larger and flatter due to reduced bleeding effects caused most likely by the absence of convection. Microgravity samples exhibited increased porosity and larger pore diameters, albeit the degree of hydration was comparable between 1g and microgravity samples [12]. Further MICS investigations on tricalcium aluminate (C_3A) and gypsum pastes with a w/c ratio of 1.0 showed that microgravity also affected early hydration in these systems [13]. In C_3A–gypsum mixtures with higher gypsum content, gypsum crystals exhibited pronounced striations under microgravity. In mixtures with lower gypsum content, a thin reaction shell outlining the original gypsum morphology was observed during early hydration [13].

As part of the MICS experiments the Techshot Multi-use Variable-gravity platform (MVP) on the ISS was used to cure cement paste samples under various gravity conditions [14]. For the investigated mixture with a w/c ratio of 0.5, nanoindentation studies revealed no significant differences in micro-mechanical properties of the cement paste components with varying gravity. This suggests that the composition and structure of hydration products remain mainly unaffected by gravity. Changes in air void structures were observed with lower gravity leading to higher air void content [14].

The research on concrete in microgravity delivered valuable insight in cement hydration processes, but up to now, no data on the most important property of concrete, the compressive strength, has been measured for microgravity samples. Therefore, the MASON (Material Science on Solidification of Concrete) research project was launched to investigate the structural properties of space concrete. The project was conducted by the Institute for Structural Concrete (ISC) at the University of Duisburg-Essen (UDE), in collaboration with the Institute of Theoretical Physics at the University of Cologne (UZK) and the Institute of Medical Engineering at the Hochschule Luzern (HSLU), with support from the German Aerospace Center (DLR). A manual

concrete mixer was developed, which was used to produce overall 400 concrete or cement paste specimens, 64 of them in microgravity (µg) on the ISS. The samples were made from 20 different mixtures and exhibited a defined cylindrical shape [15]. As part of the overall project, a significant number of samples were produced under Earth gravity (1g) and simulated microgravity conditions, both for pretests and for final comparisons. In an innovative approach a clinostat (C) and a random positioning machine (RPM) were used to subject concrete to simulated microgravity [16]. Establishment of simulation technologies are of great importance for future constructions in space and constitute an important basis for building in different gravity conditions.

This study focuses on the effect of gravity on porosity and the mechanical properties of 46 cement paste cylinders made from two different mixtures. Previous investigations prompt that porosity increases in microgravity compared to ground samples [12]. The influence of the increased porosity on the mechanical properties has not been clarified in the investigations carried out so far. In addition, the behavior of air-entraining admixtures under microgravity conditions has not been explored. While terrestrial cement was used to provide a controlled baseline, extraterrestrial construction materials may differ in composition and reaction kinetics. Nevertheless, the observed trends in porosity and mechanical behavior are expected to reflect fundamental gravity-dependent effects relevant to a broader range of binder systems. This work addresses these gaps by systematically examining how both microgravity and simulated microgravity conditions affect porosity, compressive strength, and elastic moduli, providing a foundation for understanding gravity-dependent effects in binder materials and their potential implications for extraterrestrial construction.

2 Material and methods

2.1 Materials and mixture composition

In the MASON project 64 specimens made from 20 different mixtures were produced on the ISS, which varied in terms of binder (CEM I 42.5 N and 52.5 R), aggregate (quartz sand, CEN standard sand and EAC-1A regolith), and additives (air-entraining agent and superplasticizer). This study focuses on two mixtures, R and R-AEA, from which three specimens were produced on the ISS and twenty on Earth for each mixture, resulting in a total of 46 specimens investigated in this study (see Table 1). A fine grade (Blaine 5,250 cm^2/g) ordinary Portland cement CEM I 52.5 R (Milke Premium, Heidelberg Materials) was used, either with water alone (mixture R) or water with 4% air-entraining agent (mixture R-AEA, MasterAir 102, Master Builders Solutions). The air-entraining agent (AEA) based on olefin sulfonate was diluted in the mixing water to a concentration of 4% by mass of the water (approximately 160 mL per 100 kg of cement). The AEA dosage used in this study was not selected to achieve a predefined target air content, as in conventional air-entrained concrete. Instead, the maximum dosage permitted by the NASA/ISS toxicological safety assessment was used to intentionally create a distinctly modified air-void system with more pronounced pores. This enhanced the contrast between samples and enabled a more robust analysis of the influence of gravity on pore formation and distribution in cement paste.The water/cement ratio was set to 0.40. As the composition of the ISS water fluctuates, very low mineral content water with a maximum conductivity of 6 µS/cm was used for all samples. The same water source was used for the ISS, 1g, and simulated microgravity specimens to ensure comparability.

Table 1 MASON mixtures R and R-AEA (material for one MCM sample)

Mixture ID	Admixture	Cement [g]	Water [g]	Ratio w/c	AEA concentration [%]	Sample count
R	–	54	21.5	0.40	–	23
R-AEA	AEA	54	21.5	0.40	4.00	23

2.2 Sample preparation and production

2.2.1 Sample types, production and storage

Experiments on the ISS are conducted in one of the most challenging environments imaginable, with unique demands that far exceed those of terrestrial experiments. The high costs, limited sample quantities, and strict safety protocols create an exceptionally difficult situation. Space missions in materials science are inherently complex due to factors such as the need for precise control over experimental conditions, the challenge of ensuring sample integrity during transportation and storage, the limited availability of resources and equipment, and the difficulty of conducting real-time monitoring and adjustments in a remote, microgravity environment. For example, cement is considered as NASA's toxic hazard level THL-2 and thus must at all times be enclosed within three independent levels of containment to meet safety requirements on the ISS. To address these extreme constraints, the MASON concrete mixer (MCM, detailed description in [15], Fig. 1) was specifically developed, enabling the production of cylindrical concrete specimens under these demanding conditions.

With the MCM, concrete and cement paste samples were produced with a cylindrical shape of 30 mm in diameter and approximately 50 mm in length (Fig. 2). The MCM was filled with 54 g of cement and closed. 21.5 g water with or without 4% air entraining agent was injected. The components were mixed by hand for 2 min. The mixer blade was retracted and the sample compressed. During compression, excess air was displaced through an exhaust/filter system. The filter was required because the MCM had to remain a sealed containment system for ISS safety reasons and prevent the release of cement particles. A more

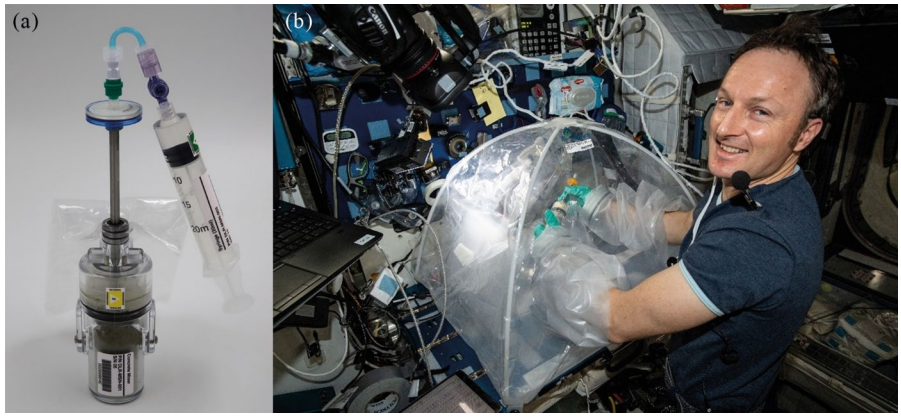


Fig. 1 **a** MASON Concrete Mixer (MCM), **b** German ESA-astronaut Matthias Maurer during the ISS experiment (credit NASA/ESA)

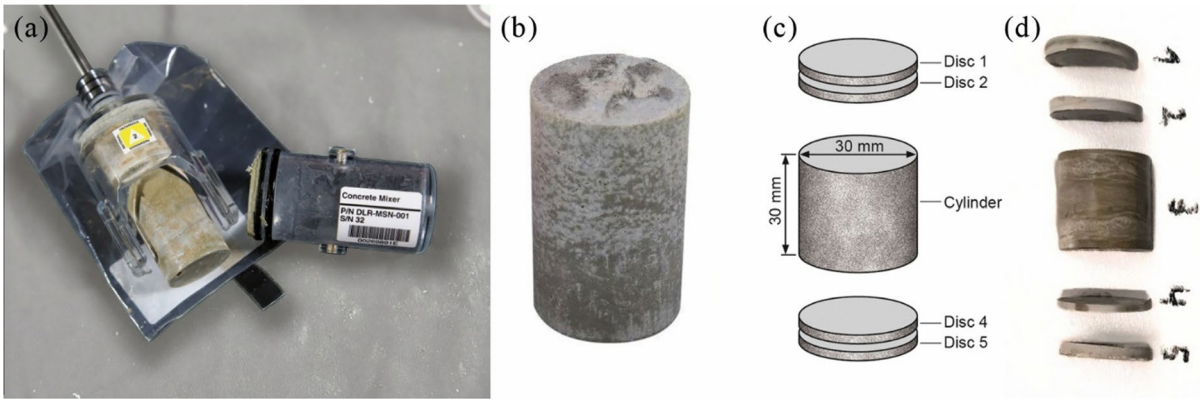


Fig. 2 **a** Extracting the sample from the MCM, **b** sample shape, **c** and **d** division of the sample

detailed description of the production process can be found in [15]. All in all, the MCM proved to be suitable for the production of concrete specimens on board the ISS in the intended way. However, if liquid reached and clogged the filter, further air displacement was hindered and the piston could not fully compress the sample to the nominal final volume.

For each mixture (R and R-AEA), five types of samples were produced and solidified under different gravitational conditions. For a complete list of the samples refer to Appendix Table 8:

(1) Earth gravity in vertical, upright position (1g-V), sample count 6 (R) and 4 (R-AEA),
(2) Earth gravity in horizontal, lying position (1g-H), sample count 6 (R) and 6 (R-AEA),
(3) Simulated microgravity in the clinostat (C), sample count 5 (R) and 7 (R-AEA),
(4) Simulated microgravity in the random positioning machine (RPM), sample count 3 (R) and 3 (R-AEA),
(5) Microgravity on the ISS (µg), sample count 3 (R) and 3 (R-AEA).

The terrestrial reference specimens were prepared in two orientations (1g-V and 1g-H) to investigate potential orientation-dependent microstructural effects caused by gravity during hardening. As no systematic differences were observed in the measured bulk properties and no microstructural analysis is included in this paper, both groups are combined and referred to as "1g" throughout the manuscript unless stated otherwise. The gravity simulators are usually used in gravitational biology [17–20] and were validated for concrete in previous investigations [16, 21]. Following the approach of these previous studies, the rotating speed and time of the clinostat was set between 5 and 50 revolutions per minute (rpm) for 24 h, while for the RPM the random walk algorithm (60°/s) was applied to simulate the effects of microgravity. The selected rotation speed depends on the convective velocity of particles and air bubbles within the investigated suspension and therefore on its viscosity. The minimum speed must be sufficiently high to keep the radius of the particle and bubble trajectories as small as possible, thereby minimizing gravity-induced motion. Conversely, the maximum speed is limited by the resulting centrifugal acceleration, which was kept below 10^{-2} g to ensure microgravity conditions. Data on the residual acceleration levels for the clinostat can be found in the Supplementary Material. The clinostat works by continuously rotating the sample around a single horizontal axis, effectively averaging the gravitational vector over time to near zero. In contrast, the RPM rotates the sample along two independent axes in a random pattern, creating a more complex motion as described in [22]. Both methods reduce the net gravitational effects on the sample, mimicking certain conditions of microgravity during the setting and early hydration phases.

For optimal comparability, all samples – ISS, 1g, C and RPM – were prepared, handled and analyzed identically with precise step-by-step protocols, only differing in the equivalent gravity during curing. Although the MCM provides a sealed environment, all samples were exposed to identical external conditions matching those on the ISS: 23±1 °C temperature and 38±1% relative humidity. After the samples were returned to the team on Earth, 287 days after mixing, the MCMs were stored in a lab with humidity control, maintained at less than 30%.

All samples were stripped, inspected and photographed from all sides and unexpected characteristics were documented. The 50 mm cylinders were labeled on the top, measured and initially weighed. After 301 days of curing, the samples were soaked in isopropanol to displace residual water and stop hydration [23–25]. The samples remained in isopropanol for 6 weeks and the weight under buoyancy was determined. Afterwards the samples were dried in an oven at a maximum temperature of 40 °C until constant mass was reached and the dry weight was determined. This gentle drying of the samples was used to avoid damaging hydration products such as ettringite [26]. To eliminate the possibility of carbonation, the samples were then stored in sealed containers filled with nitrogen [25]. The humidity in the storage chamber was maintained at below 30%. A detailed timeline of sample processing is provided in the Supplementary Material.

2.2.2 *Sample processing and precision cutting*

After extracting the sample from the MCM, the initial inspection and the non-destructive tests on the untreated 50 mm cylinders were done (for process overview see Table 2). Subsequently, the samples were cut as depicted in Fig. 2: a cylinder of 30 mm

Table 2 Overview of the methods

No	Method	Sample state	Description
1	Inspection, survey and weighing	complete cylinder and cut cylinder	Specification of external characteristics, weight, dimensions and bulk density
2	Calculation of total porosity	complete cylinder and cut cylinder	With bulk and skeletal density [23]
3	Helium pycnometry	Fragments, ground (5–6 g)	Determination of skeletal density
4	Ultrasonic measurements	complete cylinder	Identification of local, large defects, stiffness, E-modulus, differences in upper, middle and lower sample parts
5	Computed tomography	complete cylinder	Complete 3D record of distribution of mixture ingredients. Identification of air pore shape, sizes and content ≥ 96 µm pore diameter
6	Mercury intrusion porosimetry	Fragments, crushed (2 g)	Distribution of air pores ≥ 3.6 nm to approximately 112 µm diameter
7	Determination of air pores on discs	30 mm discs (complete cross-sectional area)	Examination of cross-sectional area to study distribution of mixture ingredients. Identification of air pore shape, sizes and content ≥ 10 µm diameter
8	Uniaxial compression tests	cut cylinder	Determination of compressive strength

length and 4 cross-sectional discs of 2–3 mm thickness, 2 from the top and 2 from the bottom. The slices were cut using a Struers Secotom 50 automatic precision cutting machine with a 0.40 mm slim diamond blade and waterless coolant, minimizing stress buildup. The slices were ground using silicon carbide wheels with different grit sizes and isopropanol as a lubricant as described in [21].

2.3 Experimental methods

2.3.1 Overview

As microstructural changes in cementitious materials under microgravity have been investigated in previous studies [12], this work concentrates on bulk properties—namely porosity and strength—which are decisive for structural performance and can, for the first time, be quantified using well-defined cylindrical specimens. The experimental methods used to assess the effects of different gravitational conditions on pore structure and mechanical behavior are summarized in Table 2.

As the pore system has a considerable influence on the properties of the hardened concrete [27–30], the pores must be recorded for the entire size range of the pores. For different pores sizes, various test methods must be used [31]. The capillary pores, which are particularly indicative of the strength due to their cross-linking, can be assumed to spand the. 10 nm to 10 micron range [17, 32, 33]. The analysis methods used and optimized here are suitable for detecting the pore system from a few nanometers up to several millimeters (see Fig. 3). The experimental setup is shown in the Supplementary Material.

2.3.2 Determination of bulk density, skeletal density and total porosity

The porosity (P) is calculated using the bulk (ρ_b) and skeletal density (ρ_s) [17] with

$$P = 1 - \rho_b/\rho_s \quad (1)$$

The measurement of the bulk density according to DIN 66137-1 [34] requires the determination of both mass and bulk volume, where the mass is measured after stripping and drying (balance accuracy 0.01 g, digital caliper accuracy 0.01 mm). For cement paste specimens, the bulk volume, consisting of solid and pore volume, is calculated from the measured diameter and height according to DIN 12390-7 [35]. Skeletal density is determined from ground fragments of the sample by the pycnometer method, using helium displacement and the Boyle-Mariotte law (Porotec Pycnomatic-ATC, accuracy ±0.01%, balance with ±0.0001 g). Volume determination by immersion weighing in isopropanol based

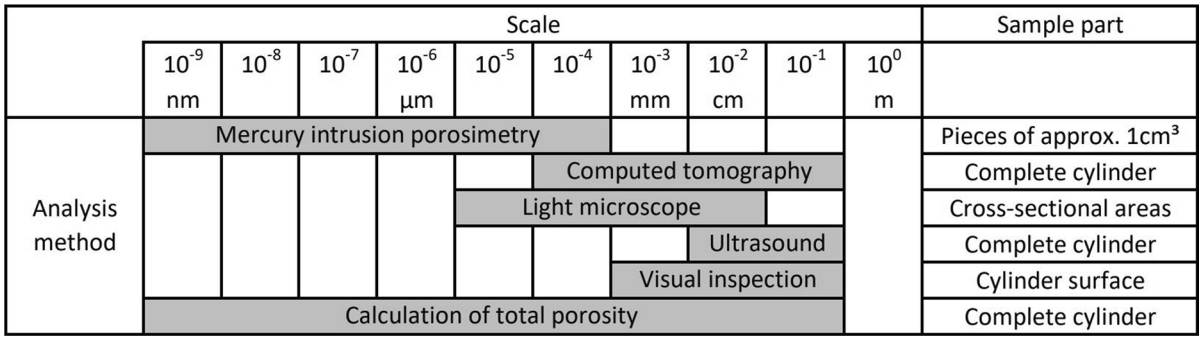


Fig. 3 Pore scales and corresponding analysis methods used in this study

on Archimedes' principle is also used as a control. This method provides a measure of the open (helium-accessible) porosity of the entire cylinder.

2.3.3 Ultrasonic measurement

The ultrasonic measurements were performed similar to DIN EN 12504-4 [36] at DLR Cologne using a digital oscilloscope with built-in signal generator (Picoscope 5000), a bipolar high-frequency/high-voltage linear amplifier (Cosinus HSA-4011), a pre-amplifier with high-pass filter (Olympus 5682) and Picoscope 6 software. Following Maruyama's approach [37], 1.8 MHz P-wave pulses were applied in radial and longitudinal direction to the cement paste specimens and measured in transmission. Radially, 24 measurements (8 measurement points each at the top, center and bottom, see Fig. 7) and one measurement per cement paste cylinder in the longitudinal direction were performed. The piezo transducer and receiver (Panametrics V103-RM) had a diameter of 13 mm and were coupled to the sample with high-viscosity (200,000 cSt) silicone oil. The time-of-flight was determined from the first arrival using a small threshold applied to normalized data. The length/thickness of the sample was measured separately for each position using a caliper. The ultrasound attenuation provided information about defects, where extremely weak received signals indicate the presence of large voids (>> 1mm) between emitter and receiver. The data allowed calculation of (P-wave) sound speed c_p and dynamic modulus of elasticity by

$$E_{dyn} = \frac{(1+\nu)(1-2\nu)}{1-\nu} c_p^2 \cdot \rho \tag{2}$$

based on the Poisson ratio $\nu \approx 0.2$, here assumed constant and equal for all mixtures after long-duration hardening, in-line with [37], and density (ρ). As the actual Poisson ratio may depend on the detailed composition of the sample [36], a dedicated investigation using shear wave measurements may be performed in the future.

The ultrasound measurement uncertainty is a statistical uncertainty from the errors in time-of-arrival of the excitation signal $\delta t = \pm 0.01 \mu s$ and the received signal $\delta t_2 = \delta t$, both measured via digital oscilloscope at a threshold of 4% of peak height, as well as from the length $\delta L = \pm 0.5$ mm and diameter $\delta D = \pm 0.05$ mm, measured via caliper. The larger error for the cylinder length results from uneven geometry of the top end of the samples. Since the radial measurements were more accurate, due to the highly reproducible diameter amongst all MCM samples, only these results are shown in Fig. 7 and 8. The overall error from Gaussian error propagation, via

$$\frac{\delta c}{c} = \sqrt{2 \cdot \left(\frac{\delta t}{\Delta t}\right)^2 + \left(\frac{\delta D}{\mathrm{D}}\right)^2} \tag{3}$$

is 0.2% for typical $\Delta t \approx 8 \mu s$ and $D \approx 30$ mm. For typical $c \approx 3.5$ km/s this gives $\delta c \approx 0.009$ km/s. It should be noted that the measured spread in times-of-arrival for different positions at the same sample is usually between 0.1 and 0.3 μs and the spread between different samples of the same mixture and setting conditions (without severe defects obstructing the ultrasound transmission) is usually within 0.2 μs, which are both much larger than the measurement error δt.

2.3.4 Computed tomography

Computed tomography (CT) was used to create digital three-dimensional volume images of entire cement paste samples to identify the open and closed pore system and local defects [39]. A Zeiss Metrotom 1500 with a tube voltage of 210 kV, a projection number of 3000 and the reconstruction algorithm according to Feldkamp was employed for the CT investigations. Tomograms of four cement paste cylinders (50 × 30 mm) could be generated with a resolution of 39 µm in 30 min per scan with a measurement uncertainty of 0.6 µm as established by the last calibration of the CT system.

The porosity of cement paste samples is evaluated by first applying a bilateral filter to reduce Gaussian noise while preserving pore edges. Afterward, the voxels are binarized using Otsu's method to separate the solid phase from voids, allowing for the calculation of solid volume. Porosity (P) is then determined by

$$P = 1 - V_s/V_t \tag{4}$$

where V_s is the solid volume and V_t is the total volume. The individual pore volumes and surface areas are computed using a marching cubes algorithm, enabling the calculation of pore sphericity (ψ) based on surface area (Sa_p) and pore volume (V_p) [40]:

$$\psi = \sqrt[3]{36\pi V_p}/Sa_p \tag{5}$$

A minimum pore size of 9 voxels is applied to the sphericity data to avoid capturing flawed aliasing behavior caused by insufficient data points.

A sensitivity analysis was conducted on the banalization method to evaluate its robustness for the given samples. The method proved to be highly reliable: when the threshold value was varied by ±5%, the resulting porosity changed by no more than +2% or −1%. The most sensitive responses were observed in the AEA samples, which also exhibited the highest density variation. Intensity histograms confirm that the selected threshold consistently falls within the valley between the peaks representing solid and void phases. Since the threshold was determined using a uniform algorithm across all samples, the segmentation procedure remains consistent and comparable across the dataset. Also the defect analysis using threshold values with the VGSTUDIO MAX software [41] was used for some samples to verify the evaluation method (see [21]).

2.3.5 Mercury intrusion porosimetry

For determining the pore size distribution of cement paste samples using mercury intrusion porosimetry (MIP) [23, 25], fragments – obtained from the compression tests – with a volume of approximately 1 cm^3 and a mass of about 2 g are taken from the core of each sample and first dried for four weeks in a desiccator containing silica gel. After reaching mass consistency, the fragments are carefully crushed to a suitable size for analysis. Then the fragments are placed in the sample container of the porosimeter, the air is evacuated and afterwards filled with mercury. The pressure is increased continuously or gradually to force the mercury into the pores. The Washburn equation

$$r_p = 2\gamma cos\theta/\Delta p \tag{6}$$

is used to determine the pore size distribution via the relationship between the pressure (Δp) and the amount of mercury [42]. The surface energy density γ of the mercury is set to $\gamma = 0{,}480 N/m$ and the interfacial angle of $\theta = 140°$ is used to determine the pore radius (rp), which are commonly adopted values for MIP analysis of cementitious materials [42]. The Washburn equation assumes idealized circular cylindrical pores and this assumption is acceptable here because MIP is used for comparative evaluation of similar specimens [43].

For the MASON samples, the MIP measurements were carried out with the Pascal 140/440 porosimeter from Thermo Scientific Fisher in accordance with DIN-ISO 15901-1 [44]. A maximum pressure of 400 MPa via a low- and high-pressure unit was applied. Thus, pores from 3.6 nm to a maximum diameter of 112 µm could be recorded. Two fragments from each sample were used for the MIP.

2.3.6 Inspection of disc surfaces with high resolution scans and automated pore detection

The blank, polished disc surfaces were scanned using an Epson Perfection V600 scanner at 4800 dpi (resolution of 5.29 µm) and the result saved in the png format. With this resolution, details on the surface can be examined at around 50× magnification.

An automated procedure, similar to [45] and detailed in [46], was employed for the air pore analysis of the discs. The ground sample surfaces were

colored black using a permanent marker (Edding 850), pressed into white barium sulfate powder with an average grain size of approximately 2 µm, and rotated to fill the pores. After removing the excess powder with a silicone spatula, the prepared sample was scanned a second time. The analysis was performed with a Matlab code developed at the ISC and provided the pore content and distribution over the cross-sectional area in a few seconds. Based on [46, 47], threshold values between 75 and 95 were selected and validated by manually counting the air voids in microscopic images (Keyence VHX-7000N microscope). In contrast to the conventional air void determination of hardened cement paste according to the standards [48, 49], no lines were drawn, but the entire cross-sectional area was evaluated. From each sample, 6 disc areas were examined, 3 from the upper and 3 from the lower part of the cylinder, with a total area of. $A_{total} \approx 6 \cdot 700 = 4200 mm^2$.

2.3.7 *Compressive strength tests*

The compressive strength of the cylinder samples was determined using destructive, uniaxial compression tests in accordance with DIN EN 12390-3 [50] and a test device specification in accordance with DIN EN 12390-4 [51]. The specimen was centered on the compression plate and loaded at a rate of 0.6 MPa/s to failure. The compressive strength (f_c) can be calculated from the fracture load (F) and the cross-sectional area of the specimen (A_c) with

$$f_c = F/A_c \tag{7}$$

2.4 Statistical evaluation

Statistical analyses were conducted to assess differences in compressive strength, porosity and elastic properties among gravity conditions (1g, clinostat, RPM, and µg) and mixtures (R and R-AEA). One-way analysis of variance (ANOVA) was used to evaluate overall differences between groups, followed by Fisher's Least Significant Difference (LSD) test for pairwise comparisons where ANOVA indicated significance [52]. Due to the limited number of replicates, differences were considered significant at $p < 0.05$.

3 Results

3.1 Sample inspection and shape

The inspection of the MCMs returned from the ISS revealed that samples R-34, R-AEA-56 and R-AEA-57 were not fully compressed due to filter clogging. Here the fresh cement paste occupied a larger volume assisted by the absence of gravity. Samples that were not fully compressed were not excluded from the analysis because they represent a relevant process-related outcome of cement paste production in microgravity. The control of the final sample volume and the removal of large cavities are critical aspects of the production process. Whenever their properties differ clearly from those of the fully compressed samples, their results are shown or discussed separately. Otherwise, they are included in the overall dataset to represent the complete outcome of the ISS experiment.

The µg-samples that were not fully compressed are significantly longer (+10 mm), larger in volume and have local defects or large cavities in some areas (see Fig. 4). Apart from this anomaly, no other different external characteristics were found in the samples of the mixtures examined here. All fully compressed samples from these mixtures look similar irrespective of their gravity state.

3.2 Computed tomography

With the CT analysis, it is possible to examine the interior of the cement paste samples. The pore size distribution and sphericity were determined by the method described in chapter 2.3.4, allowing pores with a volume of 0.000524 mm^3 or equivalent sphere diameter greater than 100 µm to be detected. The pores can be visualized so that a general distribution can be seen directly (Fig. 5).

As expected, the 1 g samples of mixture R showed the lowest porosity (Fig. 6), with predominantly small pores and only a few larger ones (diameter > 2 mm) concentrated near the top of the sample (Fig. 5). In contrast, the R µg samples exhibited a much higher porosity with numerous larger pores distributed relatively uniformly throughout the height of the sample, as anticipated based on observations from previous microgravity experiments [12]. These pores were generally more spherical. The simulation results for the R C and R RPM samples effectively replicated the pore distribution seen in

microgravity, both showing more and larger pores compared to the R 1 g samples. However, differences in sphericity were observed: while the R C samples matched the R µg samples, the R RPM samples exhibited fewer spherical pores, even less than the R 1 g samples. This is likely because uniform rotation in the clinostat facilitated better formation of spherical pores compared to the random, abrupt movements of the RPM.

With the addition of the AEA, the results changed significantly. As expected, the R-AEA 1 g samples developed far more pores (approximately +180%, Fig. 6), with buoyancy-driven accumulation towards the upper regions of the sample (Fig. 5). This upward pore migration was not observed in the R-AEA µg, C, or RPM samples, which instead showed surprisingly a lower overall porosity. The pore size distribution of the R-AEA 1 g and µg samples was very similar. The distribution of the pores in the R-AEA µg samples remained directionally uniform, but there were more pores near the bottom, while the R-AEA C and RPM samples displayed an even distribution with some larger pores in the center. Pore shape was relatively consistent across the R-AEA µg, C, and 1 g samples. However, the RPM produced the least spherical pores. This suggests that the changing direction of the motion influences the sphericity of the pores.

3.3 Ultrasound

The ultrasonic measurement was used to identify local defects such as large pores and provide insight into cement paste quality aspects such as homogeneity, porosity, hardness and density [53, 54]. A higher sonic velocity corresponds to a higher hardness or density of the material. Low sound velocities indicate higher porosity [37]. The values exceeding the scale of approximately 3.2 to 4.0 km/s are associated with local defects and larger voids [55].

The mean values of all measurements for each sample type of both mixtures are shown in Fig. 7. As expected, the 1g samples show the highest sound velocities for R (light bars, 3.89 km/s), while the values for the R µg samples (3.79 km/s) are lower due to the higher porosity. The velocities of the samples produced under simulated microgravity are also lower, with the values for the R C samples (3.77 km/s) being slightly below and those for the R RPM samples (3.84 km/s) slightly above the values for the R µg samples. ANOVA followed by Fisher's LSD test revealed no significant differences among the R sample types.

As expected, the measured ultrasonic velocities of the R-AEA samples (Fig. 7, dark bars) are generally lower than those of the R samples. The ultrasonic velocities of the R-AEA C samples (3.49 km/s) are identical to those of the 1g samples, while the RPM samples (3.62 km/s) show intermediate values between the 1g and µg samples. Notably, the R-AEA µg samples exhibit the highest velocities (3.73 km/s), whereas the 1g samples have the lowest; this difference is statistically significant. These findings are consistent with the porosity results, as the R-AEA 1g samples displayed higher porosity compared to the R-AEA µg samples.

From the individual measurements of the ultrasonic velocities, conclusions can be drawn about the composition of the sample in different areas. The 8 radial measurements were averaged so that four velocities per sample per region (top (grey), center (orange), bottom (blue), Fig. 7) are shown in the diagrams (Fig. 8). The results for the 1g samples of both mixtures illustrate the influence of the degree of compression after mixing in the MCM. Samples R-V-7 and R-AEA-V-7 were fully compressed, whereas samples R-V-10 and R-AEA-V-8 were only partially compressed. In the latter case, the mean ultrasonic velocity is slightly lower, which can be attributed to the lower compression. In addition, the values for the upper sample area are the lowest, suggesting a higher porosity due to buoyancy. This results in a plausible velocity gradient for these uncompressed 1g samples with the lowest values at the top and the highest values at the bottom. In contrast, the two compressed 1g specimens show an inverse gradient. Due to the compression in the MCM, the upper part of the sample is obviously more compacted than the lower part and therefore the highest velocities for these samples are at the top.

A compressed sample (R-33 and R-AEA-58) and a non-compressed sample (R-34 and R-AEA-57) were also selected for the µg specimens. It is evident that many values for the non-compressed samples exceed the scale (missing in Fig. 8) and that these specimens contain some big voids.

Table 3 Mean Dynamic Young's modulus calculated from ultrasonic measurements for different sample types in [MPa]

Mixture	1 g-V	C	RPM	µg	1 g/µg
R	26,683	25,597	26,420	25,301	1.05
R-AEA	19,190	19,730	21,830	23,591	0.81

*With skeletal density determined from the CT-Scans, transverse strain coefficient 0.2



Fig. 4 External appearance of **a** R-AEA and **b** R samples. **a** from left to right: 1 g-V (R-AEA-V-9), 1 g-H (R-AEA-H-8), C (R-AEA-C5-7), RPM (R-AEA-RPM-2) and µg-samples (R-AEA-58, R-AEA-57, R-AEA-56). **b** from left to right: 1 g-V (R-V-9), 1 g-H (R-H-10), C (R-C5-5, clinostat), RPM (R-RPM-2) and µg-samples (R-32, R-33, R-34)

For mixture R, all compressed samples show similar distributions for the different sample types (1g, C, RPM, µg). For the mixture R-AEA, on the other hand, larger variations in the values for the RPM and µg samples can be recognized, which indicates a higher inhomogeneity of the components. The C samples generally show the lowest variation, which are evidently very homogeneous in composition due to the defined rotation.

The calculation of the dynamic Young's modulus (Table 3) clarifies the results of the ultrasonic measurements. While the 1g samples show the highest and the µg samples the lowest value for the mixture R, the opposite trend can be observed for R-AEA. The values under simulated microgravity are for both mixtures in between and show that the simulation changes the 1g values in the desired direction and approximates the results of the µg samples. ANOVA followed by Fisher's LSD test showed only a significant difference between R-AEA 1g and µg samples. It is also important to note that the dynamic Young's modulus is sensitive to variations in the transverse strain coefficient (see Supplementary Material) and was calculated here based on an assumed value of 0.2 for all samples.

3.4 Bulk density, skeletal density and total porosity

After the CT scans and ultrasound measurements the samples were cut to discs and 30 mm cylinders as described in Sect. 2.2.2. The bulk densities of the 30 mm cylinders were calculated by measuring the dry mass and the bulk volume. For mixture R, the 1g samples exhibited the highest mean density (1.812 g/cm^3), while the R µg specimens showed the lowest mean density (1.590 g/cm^3), a difference that was statistically significant (Fig. 9a). The density values of the samples produced by microgravity simulation (R C and R RPM) were positioned in between the R 1g and R µg specimens (no statistically significant differences). When considering only the fully compressed R µg samples the mean density (1.681 g/cm^3) was higher, but still lower than the density of the other R sample types.

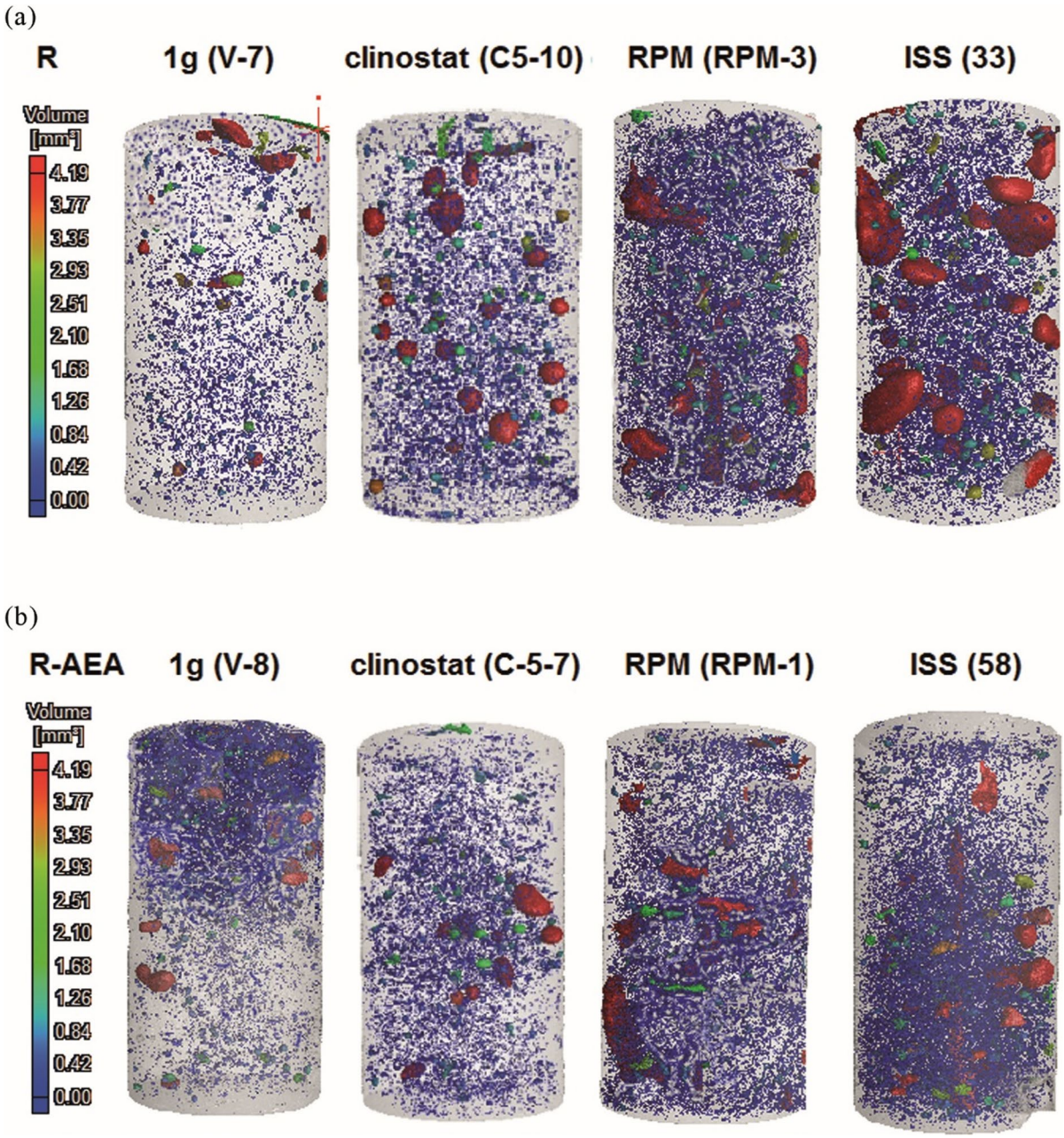


Fig. 5 Transparent 3D perspective from the CT scans of the samples of mixture **a** R and **b** R-AEA. R samples (top) from left to right: 1 g (V-7), clinostat (C-5-10), RPM (RPM-3), ISS (µg sample 33). R-AEA samples (bottom) from left to right: 1 g (V-8), clinostat (C-5-7), RPM (RPM-1), ISS (µg sample 58). The pores are shown in color depending on their size. All pores with a volume smaller than 0.52 mm^3 or an equivalent spherical diameter of approx. 1 mm are colored blue, while the pores between 1 and 2 mm are shown in a rainbow color gradient from blue to red. Pores with a volume greater than 4.19 mm^3 or an equivalent sphere diameter greater than 2 mm are shown in red

The specimens of the R-AEA mixture showed a different trend for the bulk density (Fig. 9a). Overall, the values for all sample types are similar, and ANOVA followed by Fisher's LSD test indicated no statistically significant differences between them. Interestingly the compressed R-AEA µg samples had

the higher bulk density (1.675 g/cm^3) than the R-AEA 1g specimens (1.634 g/cm^3). This was unexpected but corresponds very well with the results of the CT and ultrasound measurements. The density values of the R-AEA C samples were a bit lower (1.587 g/cm^3) and of the R-AEA RPM-samples higher (1.681 g/cm^3) than the density of the R-AEA 1g-samples.

Comparing the results from R and R-AEA, it is plausible that for the fully compressed samples, the mean values of the bulk densities of the sample types from R are greater than those from R-AEA. The standard deviation of the mean values of the bulk densities is lower for the R-AEA mixture than for the R mixture. For both mixtures it should also be noted

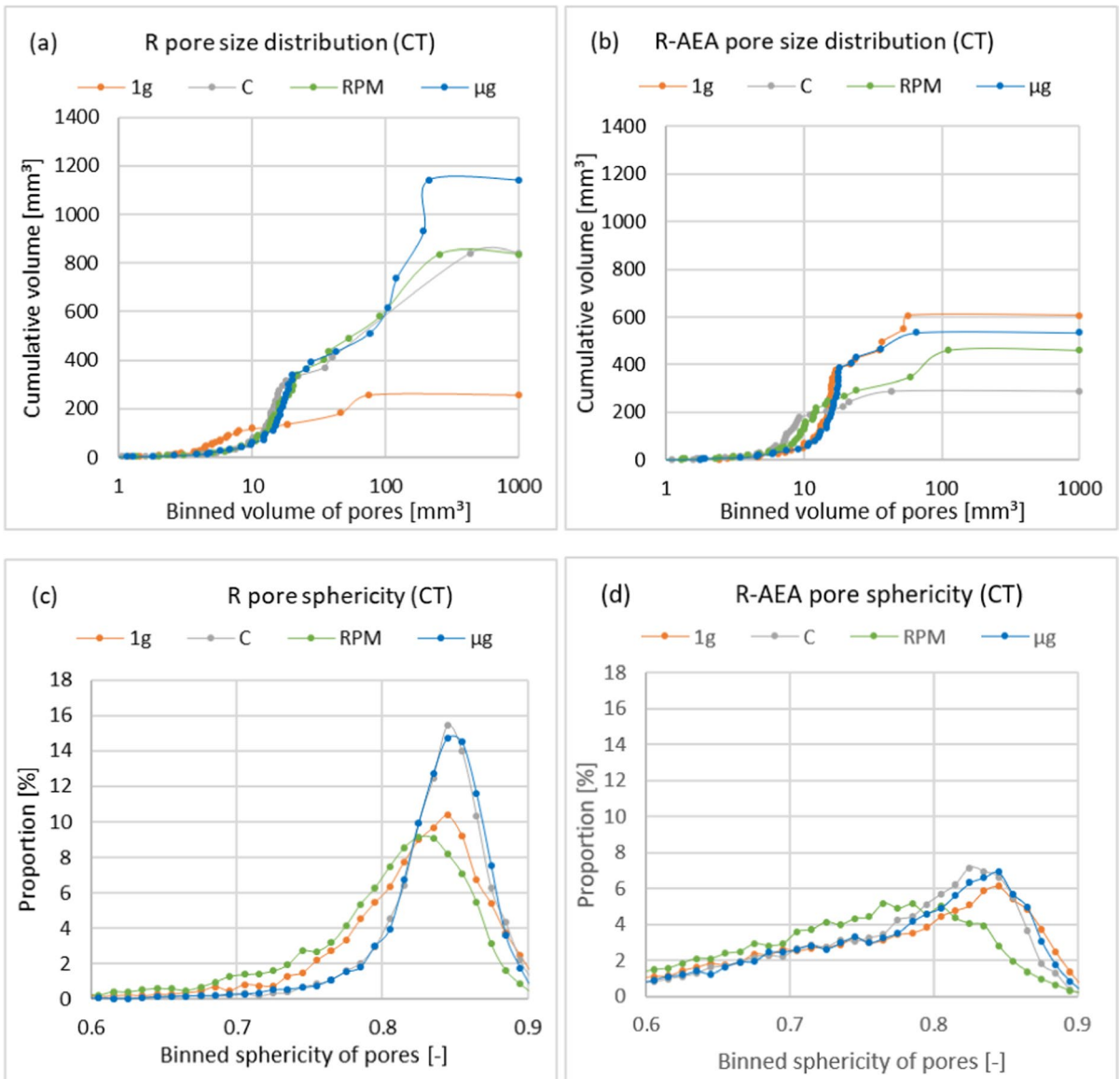


Fig. 6 Plots of CT measurement for mixtures R and R-AEA. **a** R and **b** R-AEA cumulative pore volume (mm^3, y-axis) versus binned pore volume (mm^3, x-axis) of the four sample types 1 g (orange), C (grey), RPM (green) and µg (blue). **c** R and **d** R-AEA proportion (%, y-axis) versus binned sphericity of pores ([-], x-axis) of the four sample types 1 g (orange), C (grey), RPM (green) and µg (blue)

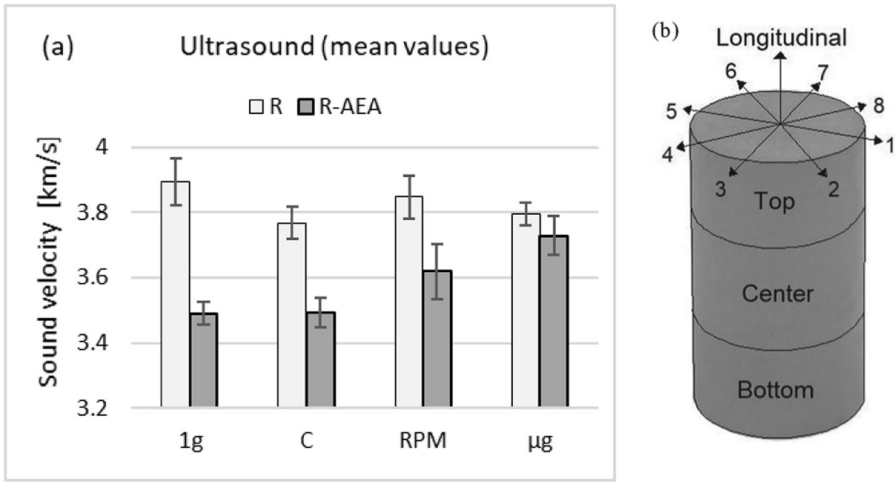


Fig. 7 **a** Mean values of the sound speed for the sample types 1 g, C, RPM and µg of the mixtures R (light grey bars) and R-AEA (dark grey bars), **b** Measurement points for ultrasound analysis

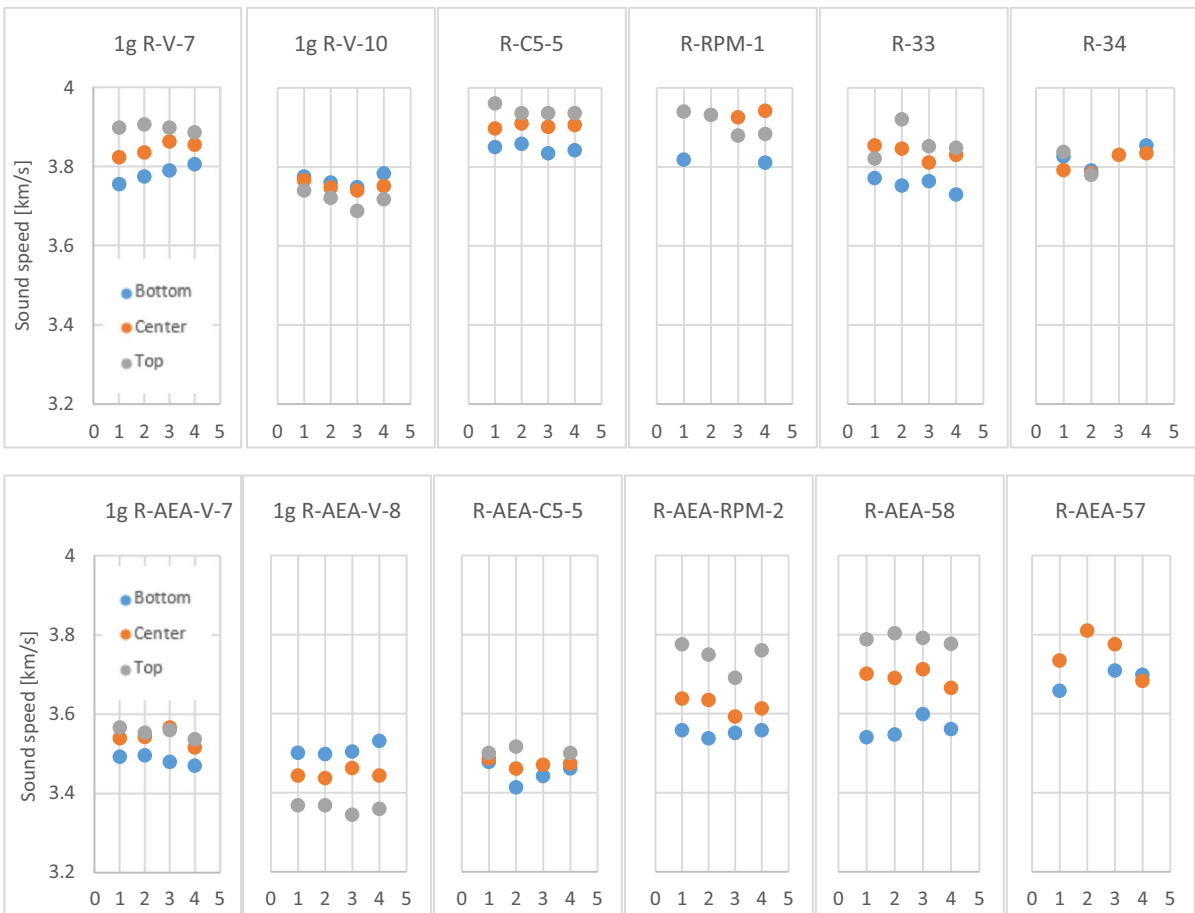


Fig. 8 Sound velocities of samples of the mixtures R and R-AEA: R-V-7 (1 g), R-V-10 (1 g, not compressed), R-C5-5, R-RPM-1, R-33 (µg), R-34 (µg, not compressed), R-AEA-V-7 (1 g), R-AEA-V-8 (1 g, not compressed), R-AEA-C5-5, R-AEA-RPM-2, R-AEA-58 (µg), R-AEA-57 (µg, not compressed). 4 measured values per area in radial direction (grey: top, orange: middle, blue: bottom) in [km/s]. Measured values outside the scale are not shown and correspond to local defects

that the uncompressed µg samples had a lower bulk density than the other µg samples.

When examining the skeletal density results (Fig. 9b), both mixtures display very similar values across the different sample types, with the exception of the R µg specimens, which have a statistically significantly lower skeletal density compared to the other sample types within mixture R.

The overall porosity results (Fig. 10) are consistent with the findings for bulk density. For mixture R, the µg samples exhibit the highest porosity (31.8%), while the 1g samples have the lowest (27.9%). However, this difference is not statistically significant. The porosity values of the simulated microgravity samples R C and R RPM specimens are in between. If only the compressed R µg samples are considered, the values (29.0%) are only slightly higher than those of the R 1g samples.

Although the porosity differences within the R-AEA samples are overall small, the porosity of the R-AEA µg samples (27.5%) is statistically significantly lower than that of the R-AEA 1g specimens (29.9%). The values of the R-AEA RPM samples correspond to those of the R-AEA µg samples, while those of the R-AEA C samples are the highest. ANOVA followed by Fisher's LSD test revealed significant differences between the R-AEA 1g and RPM samples, 1g and µg samples, as well as between the C and RPM samples and C and µg samples.

3.5 Inspection of disc surfaces with high resolution scans and automated pore detection

As an example, one slice of each sample type of the two mixtures is shown in Fig. 11. Looking at the high-resolution scans of the polished, blank slices, there are hardly any differences in the composition between the individual sample types at the magnification achieved. After inking, however, differences in pore geometry become visible (Table 4). Since only pores larger than 10 µm are recorded, the pore contents are significantly lower compared to the determination from the skeletal and bulk density according to [17].

In mixture R, the 1 g samples have the lowest pore content (2.86%) and many small pores can be detected. The distribution over the cross section is therefore very homogeneous. Slices 1 and 2, from the upper part of the cylinder, tend to have higher pore contents in the 1 g samples than slices 3 and 4 from the lower part of the cylinder (see also [16]). This demonstrates that air bubbles in fresh cement paste experience buoyancy and rise against the force of gravity under 1 g conditions, as expected. The R µg specimens have the highest pore content (6.84%, statistically significant difference), and more pores of larger diameter can be seen due to the absence of buoyancy in microgravity. The pore content of the R C and R RPM samples is also higher than that of the R 1 g samples, and there are more larger pores. Even though the total pore content is slightly lower than that of the µg samples, the pore distribution of the µg samples can be approximated with the simulation devices.

For the R-AEA mixture, the differences in porosity between the sample types are minor and do not reach statistical significance. The R-AEA 1 g specimens have the highest porosity (9.18%) and the R-AEA µg samples have the lowest (7.93%). The values of the R-AEA C and RPM samples are in between. The average pore content of the µg specimens is only that high because there were some large voids in the area of the examined slices. As a result, the pore content and pore size of the µg samples also varied widely among the individual slices. The R-AEA 1 g specimens have many more small pores, while the R-AEA µg samples have more large pores likely due to limited fluid motion and bubble coalescence in microgravity. As a result, the pore distribution across the cross-section is significantly more homogeneous in the R-AEA 1 g samples than in the R-AEA µg specimens. The samples produced under simulated microgravity also show more and larger pores.

Table 4 Mean air void content in [%] determined by automated detection on disc surfaces with standard deviation

Mean air void content in [%]					
Mixture	1 g	C	RPM	µg	1 g/µg
	[%]	[%]	[%]	[%]	[−]
R	2.86±0.43	3.19±0.82	5.48±1.21	6.84±1.98	0.42
R-AEA	9.18±0.55	8.94±0.71	8.68±1.33	7.93±1.12	1.15

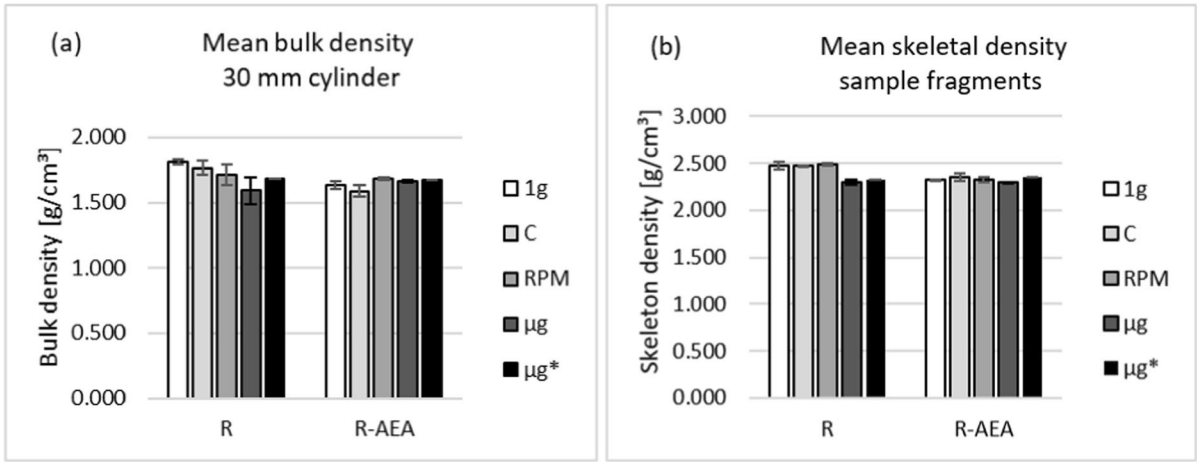


Fig. 9 **a** Mean values of the bulk densities of the 30 mm cylinders produced with MCM with standard deviation. **b** Mean values of the skeletal densities of ground sample fragments (about 5 g), determined by helium pyknometry. 1 g (white), C (light grey), RPM (grey), µg (dark grey,), µg* (black, only compressed µg samples)

3.6 Mercury intrusion porosimetry

Taking into account the limitations of the measurement method, such as the bottleneck effect and the irreversible change in the pore structure after the measurement [25, 56, 57], the MIP is suitable for comparative studies on the pore size distribution of similar concrete samples [58].

The porosity derived from MIPis shown in Table 5. For mixture R, the porosity is slightly lower in the 1g samples (19.79%) compared to the µg samples (20.92%), while higher values are observed for the R C (28.33%) and R RPM specimens (23.07%). Statistical analysis revealed a significant difference between the R C samples and both the R 1g and µg samples. The differences between the sample types are more pronounced for the R-AEA mixture. The porosity of the R-AEA 1g specimens (31.18%) is significantly higher than that of the R-AEA µg samples (21.85%). The values of the R-AEA C (24.99%) and RPM samples (23.74%) are in between. Statistical evaluation indicated a significant difference only between the R-AEA 1g samples and the other gravity conditions. The largest number of pores of a given diameter is described by the modal pore diameter, which is about 100 nm for all sample types except R-AEA 1g (about 152 nm).

More interesting, however, are the plots of cumulative pore volume versus pore diameter (Fig. 12a). For mixture R, it can be seen that the curve of the µg samples (blue) is clearly above that of the 1g samples (orange) and thus contains significantly more pores. Only for larger diameters from about 10 µm the R 1g curve rises much steeper. Up to a diameter of about 100 nm, the curves for the specimens with simulated microgravity (R C (grey) and R RPM (green)) are identical to the curve of R 1g. For larger diameters, the R RPM curve converges to the R µg curve, while the R C curve shows a very steep slope from about 40 µm.

A better correlation between the results for real and simulated microgravity can be seen for the R-AEA mixture (Fig. 12b). There the curve of R-AEA RPM (green) is almost identical to R-AEA µg (blue) and the curve of R-AEA C (grey) also shows a similar curve. The curve of the R-AEA 1g sample (orange) is interesting. Up to a diameter of about 100 nm, the R-AEA 1g curve is below the other curves, and in the range from 100 to about 1000 nm, the curve rises sharply. This means that most of the pores are present in this range, and from about 300 nm there are obviously significantly more than with the other pore types, so that the total porosity of the 1g samples is ultimately significantly higher.

3.7 Compressive strength tests

The compressive strength of concrete, which is the most important mechanical parameter, is defined as the maximum compressive stress a concrete specimen can withstand before failure. The development of cracks leading to fracture is influenced by concrete

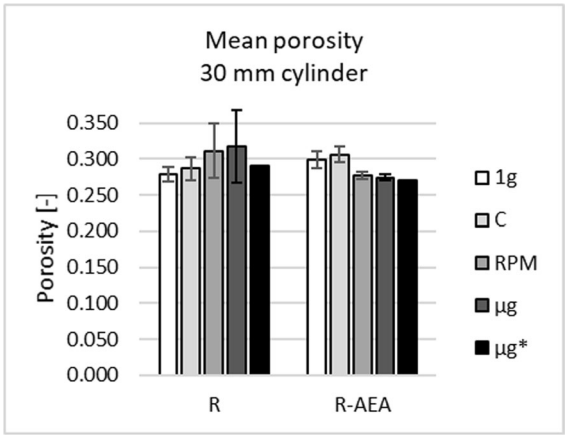


Fig. 10 Mean values of the total porosity of the 30 mm cylinders produced with MCM with standard deviation, calculated with EQ1 with the values presented in Fig. 9 for bulk and skeletal density, 1 g (white), C (light grey), RPM (grey), µg (dark grey, all samples from ISS), µg* (black, only compressed µg samples)

porosity, particularly cross-linked capillary porosity. The entire cross-sectional area is initially available for load transfer and is gradually reduced with each defect until the critical area is reached, which can no longer transfer the load [28, 59]. The larger the defect, the more the remaining area is reduced. Therefore locally larger pores have a greater influence on the strength than many small pores [60]. In the context of studying the impact of microgravity on compressive strength of cement paste samples, the MASON samples were the first examined at the macroscopic level using cylindrical specimens.

Compressive strength testing of hardened cement paste is known to exhibit greater scatter than standardized mortar or concrete tests. Previous studies reported coefficients of variation of up to 10% for cement paste [61], compared with approximately 7% for standardized mortar tests according to ASTM C109/C109M [62]. Therefore, strength differences below this level are interpreted cautiously, particularly given the small specimen size and limited number of samples.All tested samples were cured for 301 days, dried with isopropanol and moderate heating at 40°C, and stored in sealed nitrogen containers, where no further significant hardening does occur due to the lack of available water for hydration. Following the completion of all nondestructive tests, the pressure tests were conducted when the samples were between 548 and 564 days old. The mean values of the compressive strengths of the C, RPM and µg samples of mixture R were similar (around 55 MPa), while the mean value of the 1 g was significantly higher (104.19 MPa, Fig. 13a). Statistical evaluation confirmed that the 1 g samples differed from all other gravity conditions, while no significant differences were detected among the C, RPM, and µg samples for mixture R. The difference in the compressive strengths can be plausibly explained by considering the overall porosity of the individual samples. Specimens with high porosity exhibited correspondingly low compressive strengths, resulting in an almost linear progression between porosity and compressive strength of the same sample type (Fig. 13d). In addition, the samples with high porosity also had an increased number of larger air voids further reducing compressive strength. The 1 g-V (107.39±9.62 MPa) and 1 g-H specimens (100.99±7.62) had a similar compressive strength and the same porosity (0.268±0.01). The highest strength of the µg samples was 84.54 MPa (R-32) with a porosity of 0.273. Similar strengths to those of the µg samples were achieved with both the RPM and the clinostat at the same level of porosity.

For the R-AEA mixture, compressive strength values are more comparable across the different gravity conditions. As shown in Fig. 13a, the R-AEA µg and RPM samples display higher mean compressive strengths (approximately 66 MPa) compared to the R-AEA C and 1 g samples (55.99 MPa and 53.29 MPa, respectively). However, one-way ANOVA followed by Fisher's LSD post hoc test revealed no statistically significant differences among all R-AEA gravity conditions. Notably, when considering only the fully compacted R-AEA µg samples, the mean compressive strength increases to 75.87 MPa, which isa significant difference compared to the R-AEA 1 g samples. Looking at the individual values and taking overall porosity into account (Fig. 13e), there is good consistency between the R-AEA C, RPM and µg samples. The compressive strengths of the R-AEA C and RPM samples were in the range of the R-AEA µg samples with similar porosity. Overall, the R-AEA µg samples showed lower porosity and higher strengths than the R-AEA 1 g specimens. Even the non-compressed µg sample R-AEA-57 (57.63 MPa) showed

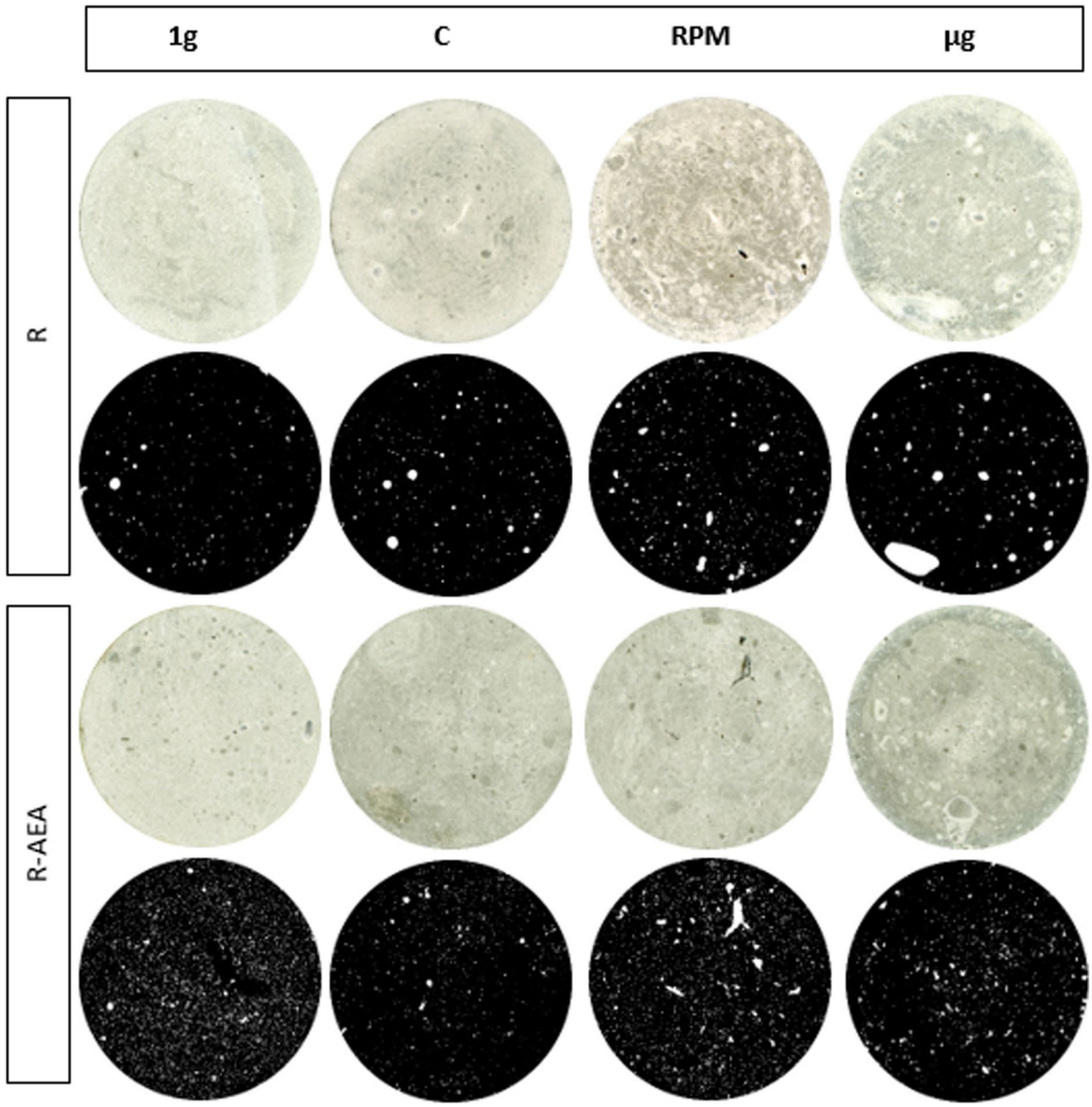


Fig. 11 Complete slice with about 30 mm diameter of the square area of the cylinders for mixtures R (top) and R-AEA (bottom). In the top rows the polished, plain surfaces can be seen and in the bottom rows the black-colored slices with the pores filled with white powder. Example slices of the sample types 1 g (first column), C (second column), RPM (third column) and µg (fourth column)

a higher strength than most R-AEA 1 g samples (53.73±6.86 MPa).

The porosity of the R-AEA 1 g samples was increased compared to the R 1 g specimens and therefore the R-AEA 1 g samples displayed lower overall strengths. Looking at the compressed samples only, the µg specimens of both mixtures have similar porosity and the R µg samples exhibit only a slight increase in compressive strength. For both mixtures, the simulation results are close to those of the µg samples.

When examining the ultimate fractures, the specimens generally displayed a failure pattern characteristic of high-strength concrete (Fig. 13b and c).

Table 5 Results of MIP: Total porosity with standard deviation and pore diameters of the four sample types 1 g, C, RPM, µg for mixtures R and R-AEA

Mixtures	Sample type	Total porosity [%]	Mean pore diameter [nm]	Modal pore diameter [nm]	Porosity value/µg [−]
R	1 g	19.79±0.49	55.51	111.78	0.95
	C	28.33±2.13	97.87	99.78	1.35
	RPM	23.07±1.17	56.15	103.66	1.10
	µg	20.92±0.89	27.73	99.18	1.00
R-AEA	1 g	31.18±1.78	89.94	152.67	1.43
	C	24.99±1.21	53.59	94.53	1.14
	RPM	23.74±1.26	43.84	106.74	1.09
	µg	21.85±0.97	34.98	102.34	1.00

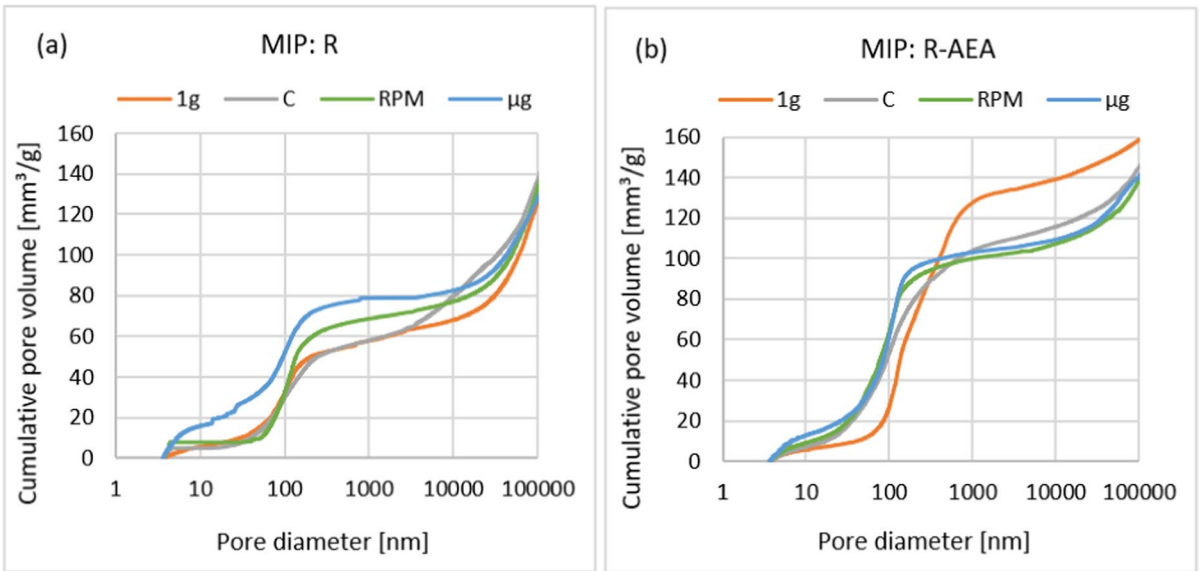


Fig. 12 Plots of MIP measurement for mixtures **a** R and **b** R-AEA: Cumulative pore volume (mm^3/g, y-axis) versus pore diameter (nm, x-axis) of the four sample types 1 g (orange), C (grey), RPM (green) and µg (blue)

In samples with significant defects, failure predominantly initiated at those defect sites, as anticipated.

3.8 Correlation of porosity measurements and mechanical properties

A range of porosity measurement techniques was applied in this study, each with distinct advantages and limitations (see Table 6 and 7). MIP provides high-resolution pore analysis but is limited to small sample fragments (approximately 1000 mm^3) and detects primarily open and connected pores ranging from a few nanometres up to 112 µm. CT, in contrast, allows quantitative assessment of the entire cylinder specimen (over 35,000 mm^3) and delivers a three-dimensional model of all pores larger than 100 µm, regardless of whether they are open or closed. Optical microscopy, although time-consuming and restricted to two-dimensional analysis of prepared cross-sections offers additional qualitative and quantitative insights into porosity, for pores larger than about 10 µm and can provide information on pore shape and distribution. The overall porosity calculation, based on bulk and skeletal densities, is a rapid and straightforward method applicable to large specimen volumes, sensitive to all open/connected pores larger than roughly 1

nm, but does not provide any information on the size distribution or morphology of the pores.

Although these methods target different aspects of the pore system and use varying sample volumes, their results generally show comparable trends with regard to sample ranking within each mixture and gravity condition. For example, in mixture R, samples with higher porosity by MIP and overall measurements also tend to have higher CT- and microscopy-derived porosity. However, systematic differences between methods are evident: CT and microscopy consistently yield lower porosity values than MIP and the overall calculation. This discrepancy arises because CT and microscopy are limited to detecting relatively large pores (>100 μm and >10 μm, respectively), missing the fine and often numerous micropores that can contribute substantially to overall porosity and are captured by MIP and density-based techniques. Furthermore, MIP and overall porosity measure only the connected/open pore space, while CT also include closed pores.

Despite differences between these techniques, the trends in porosity generally aligned with the mechanical properties. For mixture R, statistical analysis revealed a significant difference in compressive strength between the 1g samples and the other gravity conditions, while differences in dynamic Young's modulus and ultrasonic velocity were not statistically significant. In contrast, for the R-AEA mixture, a statistically significant difference in dynamic Young's modulus and sonic velocity was observed only between the 1g and μg samples; compressive strength did not differ significantly among any of the gravity conditions.

4 Discussion

4.1 Impact of microgravity on cement paste cylinder samples

For cement paste R, the microgravity samples exhibited higher total porosity and lower bulk density compared to their 1g counterparts. The absence of buoyancy in microgravity resulted in an increased content of larger, more spherical air voids uniformly distributed within the cement matrix. These findings are consistent with previous ISS experiments [12], which also reported higher porosity and altered void shapes in cement paste produced under microgravity conditions.

The microgravity environment inherently disrupts the physical processes that govern bubble movement and stability during mixing and hardening. On Earth, buoyancy causes entrapped air to rise, leading to a gradient in air void distribution and size within the cement matrix. In microgravity, the absence of this effect likely allows air bubbles to remain suspended, leading to a higher void content throughout the sample. This aligns with general principles of concrete science, where void distribution plays a critical role in determining mechanical properties and density.

The cement paste mixtures analyzed here exhibited a less homogeneous composition in microgravity compared to their 1g counterparts. However, the mixtures had a plastic fresh cement paste consistency and a stable composition (see [21]), which minimized sedimentation effects under gravity. This consistency ensured that convection-driven segregation did not dominate the results, even in terrestrial conditions. The reduced homogeneity in microgravity may be attributed to altered mixing dynamics, where the lack of gravitational forces affects the dispersion of components, including cement particles and water, during preparation.

The mechanical properties of cement paste R further corroborate these findings. The compressive strength of the microgravity samples was significantly lower than that of the 1g samples, with a clear inverse relationship between compressive strength and porosity. This trend is consistent with well-established concrete science, where higher porosity reduces the load-bearing capacity of the cement matrix by creating weak points that concentrate stress and initiate cracks. Additionally, the sound speed of the microgravity samples was notably lower, which is also in line with the observed increase in porosity.

From a scientific perspective, these results are plausible as they align with fundamental theories of concrete behavior. The relationship between porosity, density, and mechanical properties observed under terrestrial conditions can reasonably be extrapolated to microgravity.

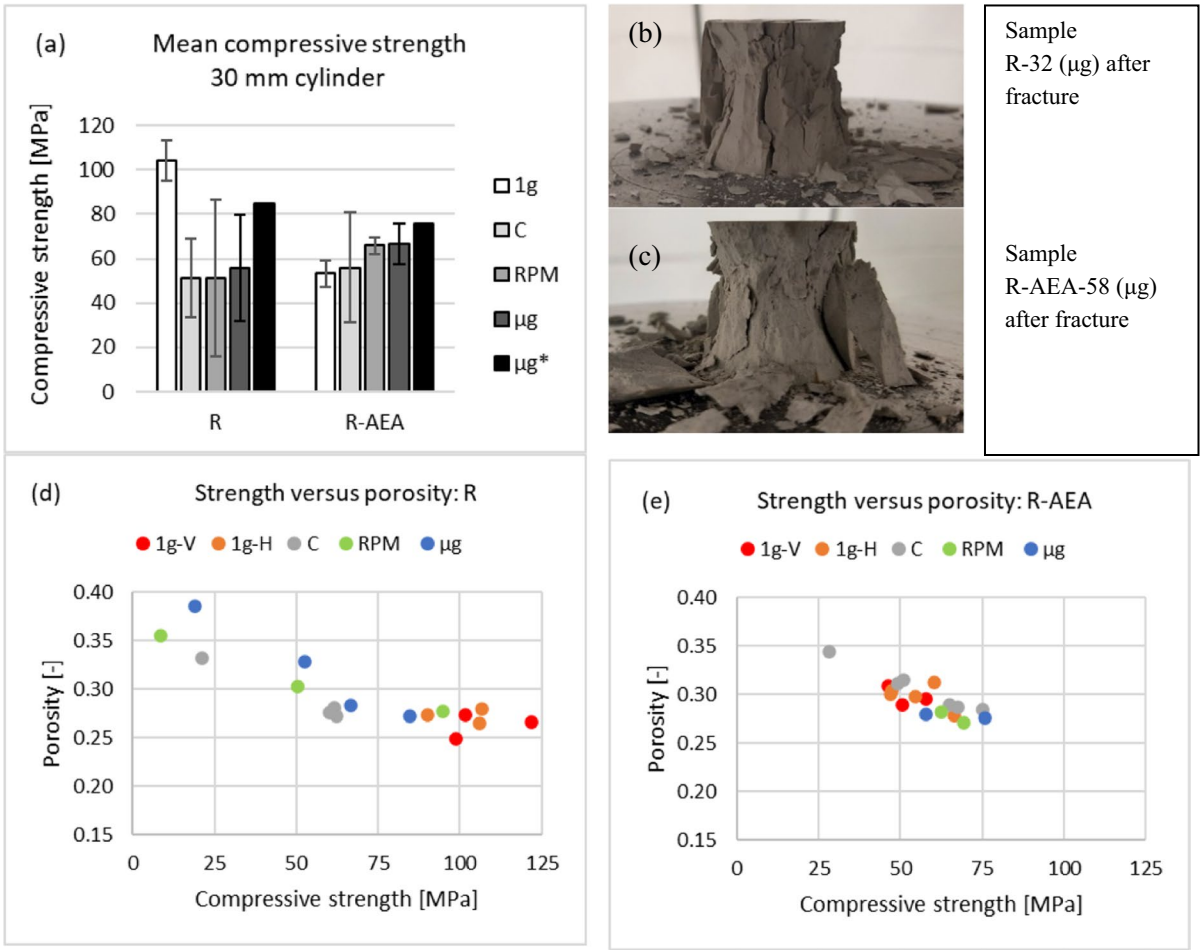


Fig. 13 Results of compressive strength test of the 30 mm cylinders. **a** Mean values of the compressive strength with standard deviation for mixtures R and R-AEA, 1 g (white), C (light grey), RPM (grey), µg (dark grey, all samples from ISS), µg* (black, only compressed µg samples). **b** Sample R-32 and **c** R-AEA-58 after ultimate failure. Compressive strength (x-axis, MPa) versus overall porosity (y-axis, see Fig. 10) for R **d** and R-AEA **e**, of the sample types 1 g-V (red), 1 g-H (orange), C (grey), RPM (green) and µg (blue)

4.2 Effect of air-entraining agent

The addition of air-entraining agent (AEA) significantly affected the properties of the R-AEA samples under both 1g and microgravity conditions, albeit with distinct outcomes:

(1) In 1g, the AEA increased porosity while reducing bulk density, Young's modulus, and compressive strength.
(2) In microgravity, however, the AEA caused less foaming, resulting in lower porosity and higher bulk density, compressive strength, and Young's modulus compared to the R-AEA 1g samples.
(3) The AEA reduced gravity-dependent differences in mechanical behavior. While mixture R showed pronounced strength differences between 1g and µg conditions, R-AEA exhibited a more consistent strength–porosity relationship across all gravity conditions. Thus, beyond its expected role of stabilizing air bubbles under 1g conditions, the AEA appears to have improved the robustness or repeatability of the specimens with respect to gravity-dependent processing effects.

The AEA based on olefin sulfonate works in gravity by stabilizing air pores within the fresh cement paste matrix [63]. As an anionic surfactant, it reduces

Table 6 Summary of results

Gravity condition	CT porosity	Microscopy porosity	MIP porosity	Overall porosity	Compressive strength	Sound velocity	Youngs modulus
	[%]	[%]	[%]	[%]	[MPa]	[km/s]	[MPa]
R							
1 g	2.40	2.86	19.79	27.90	104.19	3.89	26,683
C	2.40	3.19	28.33	28.66	51.27	3.77	25,597
RPM	7.00	5.48	23.07	31.17	51.32	3.85	26,420
µg	4.90	6.84	20.92	31.78	55.67	3.80	25,301
R-AEA							
1 g	6.80	9.18	31.18	29.91	53.29	3.49	19,190
C	3.00	8.94	24.99	30.66	55.99	3.49	19,730
RPM	6.00	8.68	23.74	27.75	65.78	3.62	21,830
µg	6.10	7.93	21.85	27.47	66.75	3.73	23,591

Table 7 Porosity specifications of measurements applied in this study

Porosity specifications				
	CT	Microscopy	MIP	Overall porosity
Sample size	35,343 mm^3	4,341 mm^2	1000 mm^3	21,206 mm^3
Pore type	All	All	Open/connected	Open/connected
Pore size	≥96 µm	≥ 10 µm	2.3 nm—112 µm	> 1 nm

the surface tension of the water, which helps encapsulate air bubbles within the paste [64]. The olefin sulfonate molecules adsorb at the air–water interface of these bubbles and contribute to the formation of a stable foam structure within the cement paste matrix, preventing the coalescence or collapse of the air bubbles [65]. This stabilization is essential for maintaining the desired air void system over time. In 1g the AEA effects concrete with improved freeze–thaw resistance but also workability and durability by reducing permeability and chloride ingress [66] leading to lower flexural and compressive strength, typically a 5–10% strength reduction per 1% entrained air [67, 68].

In microgravity, the AEA appears to be less effective due to a combination of physical and process-related factors within the MCM. In the absence of buoyancy and sedimentation, air bubbles generated during mixing cannot migrate or stabilize as they would under terrestrial conditions, resulting in a less homogeneous air-void system. The 1g reference specimens demonstrate that the MCM mixing procedure generated sufficient air bubbles for the AEA to stabilize, as the optically determined macro-air void content increased from approximately 2.9% for mixture R to approximately 9.2% for mixture R-AEA. In contrast, under microgravity, the limited mixing energy within the confined MCM chambers, combined with altered air void dynamics and potentially modified surface tension effects, likely reduced bubble stabilization and foaming efficiency despite the intentionally high AEA dosage. The FOAM project results suggest that foams are generally more stable in microgravity [69], likely due to the absence of drainage (which in 1g causes the liquid phase to drain out of the foam, leading to coalescence of bubbles) [70]. The observed correlations, such as lower porosity coinciding with higher strength and stiffness, are consistent, but the underlying mechanisms require further investigation. The AEA dosage in this study was intentionally high, and within the broader MASON project, six AEA-containing mixtures were produced in microgravity: two cement pastes and four with various aggregates. Preliminary results from the latter mixtures indicate higher densities for the microgravity samples compared to their 1g counterparts.

However, since only one AEA dosage is reported in this study, the findings should be interpreted within this limitation.

4.3 Assessment of microgravity simulation for cement paste

The R clinostat and RPM samples displayed higher porosity, larger pore sizes, and reduced compressive strength compared to the R 1g samples, closely mirroring the characteristics observed in the R microgravity specimens. For the R-AEA mixture, RPM samples demonstrated lower porosity, larger pores, and higher compressive strength than the R-AEA 1g samples, resembling the results of the R-AEA microgravity specimens. Meanwhile, the R-AEA clinostat samples generally exhibited properties closer to those of the R-AEA 1g samples, with slightly lower porosity and comparable compressive strength.

The clinostat's defined rotation contributed to enhanced compositional homogeneity for both mixtures, and the pore sphericity observed in these samples was consistent with that of μg samples. In contrast, the RPM's random motions resulted in higher heterogeneity, which often aligned more closely with actual microgravity samples for both mixtures. However, the RPM samples contained fewer spherical pores compared to μg samples, suggesting that while random motion approximates certain μg characteristics, it does not fully replicate the effect of zero gravity on bubble formation and stabilization.

Both simulation methods effectively influenced the cement paste properties and provided intermediate results between those of 1g and μg samples. However, neither fully replicated the specific effects of microgravity, such as the combination of increased porosity, pore sphericity, and mechanical property changes observed in actual μg samples. This limitation is not unexpected, as microgravity simulators can only approximate certain aspects of the complex fluid dynamics and lack of buoyancy present in a true microgravity environment [71, 72].

These observations are consistent with general concrete science, where fluid dynamics during mixing and early hydration significantly affect air void distribution, pore structure, and mechanical performance. The enhanced homogeneity provided by the clinostat's steady rotation supports theories that uniform, controlled mixing reduces segregation and promotes pore stabilization. Meanwhile, the RPM's ability to produce higher heterogeneity is linked to its random motion, which better approximates the irregular mixing behavior observed in microgravity.

While neither method fully reproduces μg effects, their results offer promising avenues for further refinement. With real microgravity data now available, simulation methods can be optimized to better predict concrete performance in partial gravity environments, such as those on the Moon or Mars.

5 Conclusion

Understanding the effects of microgravity is crucial for the development of future space construction materials. This study comprehensively analyzed the effects of microgravity on cement paste properties using cylindrical samples produced on the ISS. Before conducting uniaxial compression tests, extensive analyses of the samples were performed, focusing on their composition and air void characteristics, which significantly influence the compressive strength. The research utilized advanced techniques for pore characterization such as ultrasonic measurements, CT scans, mercury intrusion porosimetry and microscopy, offering a comprehensive view of pore distribution from a few nanometers to several millimeters. Complementary experiments under simulated microgravity (clinostat and RPM) provided insights into the validity of ground-based testing for extraterrestrial applications.

The study's key findings are:

(1) Impact of microgravity on cement paste: Microgravity led to increased porosity, reduced bulk density, and decreased compressive strength for samples without air-entraining agents (mixture R). The absence of buoyancy resulted in larger, more spherical voids, influencing the mechanical properties. These findings align with previous ISS experiments [12].
(2) Effect of air-entraining agent in microgravity: In samples with air-entraining agents (mixture R-AEA), microgravity produced unexpected results. A trend towards reduced porosity and improved compressive strength and Young's modulus was observed compared to 1g samples. The results also indicate a trend toward

improved sample homogeneity and repeatability in the AEA-containing specimens. As part of the MASON project, five other mixtures with AEA were produced in microgravity, four of which included aggregates. While the evaluation of these samples is still ongoing, preliminary results suggest that most samples exhibit similar behavior to the R-AEA mixture. These findings imply that air-entraining agents may function differently in microgravity due to altered fluid dynamics. However, the precise reasons for the reduced effectiveness of the AEA in microgravity remain unclear and will be the subject of future dedicated investigations.

(3) Assessment of microgravity simulation methods: Ground-based simulators (clinostat and RPM) provided valuable insights into microgravity effects. The RPM, with its random motion, successfully replicated heterogeneity patterns observed in µg samples, while the clinostat improved compositional homogeneity and pore sphericity. Though neither method fully replicated all µg characteristics, their combined use offers a promising framework for further refining simulation techniques, making them increasingly reliable for studying partial gravity environments on the Moon and Mars.

(4) Production of cylindrical samples in microgravity: All samples were successfully mixed using the MASON Concrete Mixer aboard the ISS. However, filter clogging during sample preparation caused incomplete compression in some cases. These incompletely compressed samples exhibited larger volumes, locally larger defects, and often higher overall porosity, resulting in properties that differed sometimes from fully compressed samples. This finding highlights that, although gravity has a pronounced effect on the material properties, the microgravity production process itself also exerts a measurable influence. The effects of these two factors cannot be clearly separated within the scope of the present study.

This study provides essential baseline data by determining macroscopic compressive strengths and conducting a detailed pore analysis of cement-containing cylinder samples, offering key insights for future extraterrestrial construction, e.g. on the moon. Within the MASON project, also various aggregates were used. While analysis of these mixtures is ongoing, initial findings suggest that moon regolith analogue shows promise as a viable aggregate for concrete production in microgravity, yielding high compressive strength. The mixing process still needs to be optimized to ensure optimal strength, but the production of high-quality concrete in microgravity appears feasible.

Acknowledgements The authors thank the German Aerospace Center which acts as the project executing organization for MASON and the ESA Safety Panel for the trusting and constructive collaboration. They furthermore want to express thanks to the laboratory staff of the Institute for Structural Concrete, the Institute of Materials Physics in Space and BIOTESC. Thanks go also to the MICS-team of Pennsylvania State University and NASA for in-depth discussion. The research presented in this paper was funded by the Federal Ministry for Economic Affairs and Climate Action of the Federal Republic of Germany, grant numbers 50WM2071 and 50WM2072. Furthermore, we acknowledge support by the Open Access Publication Fund of the University of Duisburg-Essen.

Author contributions JM prepared the initial draft of the paper. BR, TW provided important feedback and improved the structure of the paper. KT made the ultrasound measurements and prepared the related data. WW analyzed the CT scans. JM performed and evaluated all the other sample tests. All authors reviewed the paper. MS and MSH also initiated and supervised the work.

Funding Open Access funding enabled and organized by Projekt DEAL.

Data availability The data generated and analyzed during the current study are available upon reasonable request.

Declarations

Competing interest The authors declare that they have no known competing financial interests or personal relationships that could have appeared to influence the work reported in this paper. The funder of the project and the providers of materials had no role in the design of the study; in the collection, analyses, or interpretation of data; in the writing of the manuscript, or in the decision to publish the results.

Declaration of generative AI and AI-assisted technologies in the writing process During the preparation of this work the author(s) used DeepL in order to translate and improve spelling. After using this tool/service, the author(s) reviewed and edited the content as needed and take(s) full responsibility for the content of the publication.

Appendix

See Table 8.

Table 8 Sample list

Mixture **R**				
cement paste: CEM I 52.5 R + water, w/c ratio 0.40				
Sample designation	**Gravity**	**Treatment**	**Compression rate**	**Description**
R-V-7	1g	vertical	100%	solid cylinder
R-V-8	1g	vertical	100%	solid cylinder
R-V-9	1g	vertical	100%	solid cylinder
R-V-10	1g	vertical	75%	solid cylinder
R-V-11	1g	vertical	75%	solid cylinder
R-V-12	1g	vertical	75%	solid cylinder
R-H-7	1g	horizontal	75%	solid cylinder
R-H-8	1g	horizontal	75%	solid cylinder
R-H-9	1g	horizontal	75%	solid cylinder
R-H-10	1g	horizontal	100%	solid cylinder
R-H-11	1g	horizontal	100%	solid cylinder
R-H-12	1g	horizontal	100%	solid cylinder
R-C-5-5	simulated µg	clinostat 5 rpm	100%	solid cylinder
R-C-5-6	simulated µg	clinostat 5 rpm	100%	solid cylinder, some voids side
R-C-5-10	simulated µg	clinostat 5 rpm	100%	solid cylinder
R-C-25-10	simulated µg	clinostat 25 rpm	100%	solid cylinder
R-C-50-10	simulated µg	clinostat 50 rpm	100%	solid cylinder
R-RPM-1	simulated µg	RPM 90° random walk	50%	large voids (bottom)
R-RPM-2	simulated µg	RPM 90° random walk	100%	solid cylinder
R-RPM-3	simulated µg	RPM 90° random walk	80%	solid cylinder, some voids lower area
R-32	µg	ISS	90%	solid cylinder, brown spots on the surface
R-33	µg	ISS	90%	solid cylinder, brown spots on the surface
R-34	µg	ISS	0%	very long (64 mm), large voids

Mixture **R-AEA**				
cement paste: CEM I 52.5 R + water + air-entraining agent, w/c ratio 0.40				
Sample designation	**Gravity**	**Treatment**	**Compression rate**	**Description**
R-AEA-V-7	1g	vertical	85%	solid cylinder
R-AEA-V-8	1g	vertical	30%	very long (56 mm), solid cylinder
R-AEA-V-9	1g	vertical	90%	solid cylinder
R-AEA-V-10	1g	vertical	100%	solid cylinder
R-AEA-H-7	1g	horizontal	90%	solid cylinder
R-AEA-H-8	1g	horizontal	100%	solid cylinder
R-AEA-H-9	1g	horizontal	100%	solid cylinder
R-AEA-H-10	1g	horizontal	90%	solid cylinder
R-AEA-H-11	1g	horizontal	85%	solid cylinder
R-AEA-H-12	1g	horizontal	85%	solid cylinder
R-AEA-C-5-5	simulated µg	clinostat 5 rpm	95%	solid cylinder
R-AEA-C-5-6	simulated µg	clinostat 5 rpm	95%	solid cylinder
R-AEA-C-5-7	simulated µg	clinostat 5 rpm	80%	solid cylinder
R-AEA-C-5-10	simulated µg	clinostat 5 rpm	80%	long (53 mm), solid cylinder
R-AEA-C-5-11	simulated µg	clinostat 5 rpm	95%	solid cylinder
R-AEA-C-5-12	simulated µg	clinostat 5 rpm	90%	solid cylinder
R-AEA-C-25-10	simulated µg	clinostat 25 rpm	75%	long (54 mm) solid cylinder
R-AEA-RPM-1	simulated µg	RPM 90° random walk	80%	solid cylinder
R-AEA-RPM-2	simulated µg	RPM 90° random walk	80%	solid cylinder
R-AEA-RPM-3	simulated µg	RPM 90° random walk	80%	solid cylinder
R-AEA-56	µg	ISS	0%	very long (64 mm), large voids
R-AEA-57	µg	ISS	0%	very long (64 mm), large voids
R-AEA-58	µg	ISS	70%	solid cylinder

Open Access This article is licensed under a Creative Commons Attribution 4.0 International License, which permits use, sharing, adaptation, distribution and reproduction in any medium or format, as long as you give appropriate credit to the original author(s) and the source, provide a link to the Creative Commons licence, and indicate if changes were made. The images or other third party material in this article are included in the article's Creative Commons licence, unless indicated otherwise in a credit line to the material. If material is not included in the article's Creative Commons licence and your intended use is not permitted by statutory regulation or exceeds the permitted use, you will need to obtain permission directly from the copyright holder. To view a copy of this licence, visit http://creativecommons.org/licenses/by/4.0/.

References

1. National Aeronautics and Space Administration (NASA). NASA's Lunar Exploration Program Overview. Washington DC; 2020
2. Clinton RG, Edmunson JE, Effinger MR, Pickett CC, Fiske MR, Ballard J et al. (2022) NASA's Moon-to-Mars Planetary Autonomous Construction Technology Project: Overview and Status: 73rd International Astronautical Congress
3. Lin TD, Senseney JA, Arp LD, Lindbergh C (1989) Concrete lunar base investigation. J Aerosp Eng 2(1):10–19
4. Lin TD (1992) Concrete: potential material for space station. NASA - Johnson Space Center Space Res 3:259–266
5. Bury MA, Blakely JR, Jalbert LB, Mustaikis S II (1994) Concrete and mortar research aboard the NASA space shuttle. Concr Int 16(9):42–46
6. Bury MA, Jalbert LB, Mustaikis II S (1995) Taking Concrete to the Outer Limits. Concrete Construction
7. Yoshihiro M, Akira K, Nobuhiko N, Kazuya U (1998) Concrete hardening in microgravity (ConCIM): results of a microgravity experiment conducted on the Space Shuttle Endeavour. Concr J 36(1):4–7
8. Meier MR, Rinkenburger A, Plank J (2016) Impact of different types of polycarboxylate superplasticisers on spontaneous crystallisation of ettringite. Adv Cem Res 28(5):310–319
9. Meier MR, Plank J (2016) Crystal growth of $[Ca_3Al(OH)_6{\cdot}12H_2O]_2{\cdot}(SO_4)_3{\cdot}2H_2O$ (ettringite) under microgravity: on the impact of anionicity of polycarboxylate comb polymers. J Cryst Growth 446:92–102
10. Lei L, Meier MR, Rinkenburger A, Zheng B, Fu L, Plank J (2016) Early hydration of portland cement admixed with polycarboxylates studied under terrestric and microgravity conditions. ACT 14(3):102–107
11. Moraes Neves J, Collins PJ, Wilkerson RP, Grugel RN, Radlińska A (2019) Microgravity effect on microstructural development of tri-calcium silicate (C3S) paste. Front Mater. https://doi.org/10.3389/fmats.2019.00083
12. Collins PJ, Grugel RN, Radlińska A (2021) Hydration of tricalcium aluminate and gypsum pastes on the International Space Station. Constr Build Mater 285:122919
13. Collins PJ, Thomas RJ, Radlińska A (2023) Influence of gravity on the micromechanical properties of portland cement and lunar regolith simulant composites. Cem Concr Res 172:107232
14. Müller JTI, Rattenbacher B, Tell K, Rösch C, Welsch T, Maurer M et al (2023) Space hardware for concrete sample production on ISS "MASON concrete mixer." NPJ Microgravity 9(1):57
15. Müller J, Welsch T, Tell K, Rattenbacher B, Sperl M (2023) MASON: Betonerhärtung in Schwerelosigkeit – Simulationen mit dem Klinostaten. Beton Stahlbetonbau 118(6):406–416
16. Hemmersbach R, Strauch SM, Seibt D, Schuber M (2006) Comparative studies on gravisensitive protists on ground (2D and 3D clinostats) and in microgravity. Microgravity Sci Technol 18(3–4):257–259
17. Herranz R, Anken R, Boonstra J, Braun M, Christianen PCM, Geest deM et al (2013) Ground-based facilities for simulation of microgravity: organism-specific recommendations for their use, and recommended terminology. Astrobiology 13(1):1–17
18. Hauslage J, Cevik V, Hemmersbach R (2017) *Pyrocystis noctiluca* represents an excellent bioassay for shear forces induced in ground-based microgravity simulators (clinostat and random positioning machine). NPJ Microgravity 3:12
19. Wuest SL, Richard S, Walther I, Furrer R, Anderegg R, Sekler J et al (2014) A novel microgravity simulator applicable for three-dimensional cell culturing. Microgravity Sci Technol 26(2):77–88
20. Müller JTI (2024) Zum Beton in realer und simulierter Mikrogravitation
21. Wuest SL, Stern P, Casartelli E, Egli M (2017) Fluid dynamics appearing during simulated microgravity using random positioning machines. PLoS ONE 12(1):e0170826. https://doi.org/10.1371/journal.pone.0170826
22. Locher FW (2006) Cement: principles of production and use. Bau+Technik Gmbh, Düsseldorf
23. Konecny L, Naqvi SJ (1993) The effect of different drying techniques on the pore size distribution of blended cement mortars. Cem Concr Res 23(5):1223–1228
24. Scrivener K, Snellings R, Lothenbach B (eds) (2017) A practical guide to microstructural analysis of cementitious materials. CRC Press, London
25. Zhang Z, Scherer GW (2021) Physical and chemical effects of isopropanol exchange in cement-based materials. Cem Concr Res 145:106461
26. Xiao J, Lv Z, Duan Z, Zhang C (2023) Pore structure characteristics, modulation and its effect on concrete properties: a review. Constr Build Mater 397:132430
27. Luping T (1986) A study of the quantitative relationship between strength and pore-size distribution of porous materials. Cem Concr Res 16(1):87–96
28. Kolias S (1994) Investigation of the possibility of estimating concrete strength by porosity measurements. Mater Struct 27(5):265–272
29. Huan C, Zhu C, Liu L, Wang M, Zhao Y, Zhang B et al. (2021) Pore structure characteristics and its effect on mechanical performance of cemented paste backfill. Front. Mater, 8
30. Anders N (2017) Detection possibilities of pore structures. Mauerwerk 21(5):297–305

31. Gräf H, Bonzel J (1990) Über den Einfluß der Porosität des erhärteten Betons auf seine Gebrauchseigenschaften. Beton 40(7):297–302
32. Setzer MJ (1975) Zum Mikrogefüge des Zementsteins und dessen Einfluss auf das mechanische Verhalten des Betons. Zement+Beton 86:29–34
33. DIN 66137-1:2019-03, Bestimmung der Dichte fester Stoffe - Teil 1: Grundlagen. Berlin: Beuth Verlag GmbH. https://doi.org/10.31030/3031680
34. DIN EN 12390-7:2021-1, Prüfung von Festbeton - Teil 7: Rohdichte von Festbeton; Deutsche Fassung EN 12390-7:2019 + AC:2020. Berlin: Beuth Verlag GmbH. https://doi.org/10.31030/3221834
35. DIN EN 12504-4:2021-10, Prüfung von Beton in Bauwerken - Teil_4: Bestimmung der Ultraschall-Impulsgeschwindigkeit; Deutsche Fassung EN 12504-4:2021. Berlin: Beuth Verlag GmbH. https://doi.org/10.31030/3238894
36. Maruyama I, Igarashi G (2014) Cement reaction and resultant physical properties of cement paste. J Adv Concr Technol 12(6):200–213
37. Narayan Swamy R (1971) Dynamic Poisson's ratio of portland cement paste, mortar and concrete. Cem Concr Res 1(5):559–583
38. Rettinger M, Guhathakurta J, Gänz P, Simon S, Schlaich M (2022) Hinter den Kulissen - Computertomographie für modulare Segmentfertigteilbrücken. Beton- und Stahlbetonbau 117(5):343–356
39. Ahmed H, Kuva J, Punkki J (2024) Analysing entrapped pores in concrete via x-ray computed tomography: influence of workability and compaction time. Constr Build Mater 417:135322
40. Volume Graphics GmbH. VGSTUDIO MAX; 2023
41. Giesche H (2006) Mercury porosimetry: a general (practical) overview. Part Part Syst Charact 23(1):9–19
42. Gluth GJG (2011) Die Porenstruktur von Zementstein und seine Eignung zur Gastrennung: Dissertation
43. DIN ISO 15901-1:2019-03, Bewertung der Porengrößenverteilung und Porosität von Feststoffen mittels Quecksilberporosimetrie und Gasadsorption - Teil 1: Quecksilberporosimetrie (ISO_15901-1:2016). Berlin: Beuth Verlag GmbH. https://doi.org/10.31030/3031674
44. Jakobsen UH, Pade C, Thaulow N, Brown D, Sahu S, Magnusson O et al (2006) Automated air void analysis of hardened concrete — a round robin study. Cem Concr Res 36(8):1444–1452
45. Fonseca PC, Scherer GW (2015) An image analysis procedure to quantify the air void system of mortar and concrete. Mater Struct 48(10):3087–3098
46. Wong HS, Head MK, Buenfeld NR (2006) Pore segmentation of cement-based materials from backscattered electron images. Cem Concr Res 36(6):1083–1090
47. ASTM. Test Method for Microscopical Determination of Parameters of the Air-Void System in Hardened Concrete(C457). West Conshohocken, USA: ASTM International. https://doi.org/10.1520/C0457_C0457M-23
48. DIN EN 480-11:2005-12, Zusatzmittel für Beton, Mörtel und Einpressmörtel_- Prüfverfahren - Teil 11: Bestimmung von Luftporenkennwerten in Festbeton; Deutsche Fassung EN 480-11:2005. Berlin: Beuth Verlag. https://doi.org/10.31030/9659523
49. DIN EN 12390-3:2019-10, Prüfung von Festbeton - Teil 3: Druckfestigkeit von Probekörpern; Deutsche Fassung EN 12390-3:2019. Berlin: Beuth Verlag GmbH. https://doi.org/10.31030/3045735
50. DIN EN 12390-4:2020-04, Prüfung von Festbeton - Teil 4: Bestimmung der Druckfestigkeit - Anforderungen an Prüfmaschinen; Deutsche Fassung EN 12390-4:2019. Berlin: Beuth Verlag GmbH. https://doi.org/10.31030/3058507
51. Williams LJ, Abdi H (2010) Fisher's least significant difference (LSD) test. Encyclopedia of research design 218(4):840–853
52. Thomaz WdA, Miyaji DY, Possan E (2021) Comparative study of dynamic and static Young's modulus of concrete containing basaltic aggregates. Case Stud Constr Mater 15:e00645
53. Benouis A, Grini A (2011) Estimation of concrete's porosity by ultrasounds. Phys Procedia 21:53–58
54. Tell K (2021) Characterizing concrete with ultrasound and computed tomography for MASON/ Concrete Hardening on ISS Incr. 66 / CosmicKiss. MASON/MICS Workshop 3
55. Diamond S (2000) Mercury porosimetry. Cem Concr Res 30(10):1517–1525
56. Zhang Y, Yang B, Yang Z, Ye G (2019) Ink-bottle effect and pore size distribution of cementitious materials identified by pressurization¯depressurization cycling mercury intrusion porosimetry. Materials (Basel). https://doi.org/10.3390/ma12091454
57. Kumar R, Bhattacharjee B (2003) Porosity, pore size distribution and in situ strength of concrete. Cem Concr Res 33(1):155–164
58. Luping T, Nilsson L-O (1992) A study of the quantitative relationship between permeability and pore size distribution of hardened cement pastes. Cem Concr Res 22(4):541–550
59. Zhang M, Yao X, Guan J, Li L, Wang J, Qing L (2021) Study of concrete strength and pore structure model based on grey relation entropy. Materials (Basel). https://doi.org/10.3390/ma14020432
60. Lootens D, Schumacher K, Liard M, Jones SZ, Bentz DP, Ricci S, Meacci V. Continuous strength measurements of cement pastes and concrete by ultrasonic wave reflection method. Construction and Building Materials / NIST preprint
61. ASTM C109/C109M. Standard Test Method for Compressive Strength of Hydraulic Cement Mortars Using 2-in. or [50-mm] Cube Specimens. ASTM International, West Conshohocken, PA
62. Tunstall LE, Ley MT, Scherer GW (2021) Air entraining admixtures: mechanisms, evaluations, and interactions. Cem Concr Res 150:106557
63. Gagné R (2016) Air entraining agents. Science and technology of concrete admixtures. Elsevier, pp 379–391
64. Zeng X, Lan X, Zhu H, Liu H, Umar HA, Xie Y et al (2020) A review on bubble stability in fresh concrete:

mechanisms and main factors. Materials (Basel). https://doi.org/10.3390/ma13081820
65. Zhang P, Li D, Qiao Y, Zhang S, Sun C, Zhao T (2018) Effect of air entrainment on the mechanical properties, chloride migration, and microstructure of ordinary concrete and fly ash concrete. J Mater Civ Eng, 30(10)
66. GivKashi MR, Tohidloo M (2024) The effect of freeze-thaw cycles and sulfuric acid attack separately on the compressive strength and microstructure of 3D-printed air-entrained concrete. Constr Build Mater 440:137411
67. GivKashi MR, Moodi F, Ramezanianpour AM (2025) Effect of air-entraining agent on hardened properties of 3D printed concrete with emphasis on permeability and air void structure. J Mater Civ Eng, 37(5)
68. Caps H, Delon G, Vandewalle N, Guillermic RM, Pitois O, Biance AL et al (2014) Does water foam exist in microgravity? Europhys News 45(3):22–25
69. Vandewalle N, Caps H, Delon G, Saint-Jalmes A, Rio E, Saulnier L et al (2011) Foam stability in microgravity. J Phys Conf Ser 327:12024
70. Hauslage J, Abbrecht M, Hanke L, Hemmersbach R, Koch C, Hanke W et al (2016) Cytosolic calcium concentration changes in neuronal cells under clinorotation and in parabolic flight missions. Microgravity Sci Technol 28(6):633–638
71. Wuest SL, Richard S, Kopp S, Grimm D, Egli M (2015) Simulated microgravity: critical review on the use of random positioning machines for mammalian cell culture. BioMed Res Int 2015:971474

Publisher's Note Springer Nature remains neutral with regard to jurisdictional claims in published maps and institutional affiliations.